DIPLOMA THESIS

Design and Mechanical Construction of a Hot-Corrosion Testing System

by

Alexander Scheiber

[redacted]

carried out for the purpose of obtaining the degree Master of Science
under the supervision of

Univ.Ass. Dipl.-Ing. Dr.techn. Helmut Riedl-Tragenreif
Project Ass. Dipl.-Ing. Oliver Ernst Hudak

E 308 - Institute of Materials Science and Technology
Applied Surface and Coating Technology Research Group

submitted at

Technische Universität Wien
Getreidemarkt 9
1060 Wien, Österreich

Wien, November 2020

“When you come to the end of all the light you know, and it’s time to step into the darkness of the unknown, faith is knowing that one of two things shall happen: Either you will be given something solid to stand on or you will be taught to fly.”

– Edward Teller (1908-2003)

This work was supported by Plansee SE, Composite Materials GmbH, and Oerlikon Balzers, Oerlikon Surface Solutions AG in the framework of the Christian Doppler Laboratory for Surface Engineering of High-Performance Components.

Affidavit:
I declare in lieu of oath, that I wrote this thesis and performed the associated research myself, using only literature cited in this volume.

Date

Signature

Acknowledgements

First, I would like to express my gratefulness to **Dr.techn. Helmut Riedl-Tragenreif** for his supervision of my diploma thesis and the incredible support during my five years as project assistant. Many things I learned at the material science institute is credited to you and I will definitely benefit from these experiences in the future. Helmut, thank you for lending me an ear in tough situations.

Next, I want to express my personal gratitude to **Dr.mont. Paul Heinz Mayrhofer** for giving me the opportunity to be part of this fantastic working group and enable me the insight in many interesting research issues. Your motivation and interest in our research field is encouraging everyone at the institute. Also, as a student I attended all your lectures with pleasure and improved my know-how in every lesson.

I am extremely grateful for the daily support of **Dipl.Ing. Oliver Ernst Hudak** through this thesis. Thank you Oli for the countless night hours you spent for my diploma thesis. I cannot remember one day with bad mood on your side. The frequent jokes during the build-up period in the lab made work easy going.

Also, I would like to thank all members of my working group for supporting me in every situation. It was a pleasure to work with all of you on various tasks. The coffee breaks and after-work sessions were a welcome change from the daily life of being a student.

Finally, and most importantly I would like to show my deepest appreciation for my family. The great backing and encouragement from your side throughout the years cannot be expressed in words. **Mum** and **Dad**, without your unconditional support, I would have not been able to come this far – as a student and as a person. Above all, my biggest thanks go to **Susanne**, the most important person in my life. You motivated me in hard situations and encouraged me to constantly strive for the best. The contagious soulfulness of our sunshine **Mila** enforced me to be cheerful in difficult times with her never ending smiles and hugs.

Contents

List of Figures

List of Symbols & Abbreviations

ΔG	difference in Gibbs Energy
ΔH	change in enthalpy of the system
ΔS	entropy change inside the system
λ	air-to-fuel ratio
$\lambda_{\mathrm{X\text{-}ray}}$	wavelength of the X-rays
$\phi_{\mathrm{SO_2}}$	volumetric concentration of SO_2
θ	X-ray diffraction angle
$\dot{V}_{(\mathrm{max})}$	maximum flow rate inside the pipe system
$\dot{V}_{\mathrm{Ar(max)}}$	maximum argon flowrate
$\dot{V}_{\mathrm{O_2(max)}}$	maximum oxygen flowrate
$\dot{V}_{\mathrm{SO2(max)}}$	maximum sulfur dioxide flowrate
APS	atmospheric plasma spraying
BBHD	Bragg Brentano high definition
c_{Ba}	molar concentration of barium in barium standard solution 0.01 N
CFC	Corrosion fatigue cracking
CORA	Corrosive Oven for Research and technical Applications
d	lattice spacing of crystal structures
EDS	electron dispersive X-ray spectroscopy
f_{eq}	equivalence factor of barium inside the reaction
HC	hot corrosion
HiPIMS	high-power impulse magnetron sputtering
HTC	high-temperature corrosion
HTHC	high temperature hot corrosion
HVOF	high velocity oxygen fuel spraying
k_{volume}	factor for extracted volume of the diluted impinger
LTHC	low temperature hot corrosion
MFC	mass flow controller
n	integer number

N_{Ba}	equivalence coefficient of barium standard solution
n_B	quantity of barium which neutralize the solution
n_{SO_2}	quantity of SO_2 inside analyzed part of impinger 3+4
n_{SO_3}	quantity of SO_3 inside analyzed part of impinger 1
PVD	physical vapor deposition
SCC	stress corrosion cracking
SEM	scanning electron microscopy
T	temperature of system
TBC	thermal barrier coatings
v_{pipe}	maximum gas velocity inside the pipe system
$v_{reactor}$	maximum gas velocity inside the reactor
V_s	bias potential of substrate
$V_{titr(SO_2)}$	quantity of barium standard solution to neutralize SO_2
$V_{titr(SO_3)}$	quantity of barium standard solution to neutralize SO_3
XRD	X-ray diffraction

Abstract

Hot corrosion is a pressing issue in post-combustion sections of jet engines, where turbine elements suffer from accelerated corrosion in the presence of salt-deposits in SO_x-rich atmospheres. Depending on the temperature, two types of hot corrosion mechanisms have been identified throughout the past: A low temperature hot corrosion process (LTHC, 600-850°C), and a high temperature hot corrosion type (HTHC, 750 950°C). Depending on the temperature range, the salt that deposits on the material surfaces may be present in a molten or solid state, which ultimately dictates the corrosive mechanism of the material components. In order to lower maintenance and repair costs for affected component surfaces, novel materials with superior corrosion behavior against hot corrosion are in great demand.

In this regard, this thesis presents the conceptualization and construction of a Corrosion Oven for Research and technical Applications (CORA), capable of simulating hot corrosion environments as found in industrial high temperature applications. CORA was designed in three main segments: gas mixing system, reaction chamber, and gas analysis system. The composition of the corrosive atmosphere inside the reaction chamber was calibrated and controlled using three separate mass flow controllers with ranges of 5000, 500, and 10 sccm designated for Ar, SO_2, and O_2, respectively. A consistent atmosphere of 2.5 sccm (SO_2), 375 sccm (O_2) and 2125 sccm (Ar) was maintained throughout all corrosion experiment, which is equivalent to 1000 ppm SO_2 - a typical concentration often found in flue gases. A horizontal tube furnace with a quartz tube reactor was implemented, as the reaction chamber. In order to accommodate experimental conditions that support both LTHC and HTHC mechanisms, a furnace capable of reaching 1100°C was chosen. Furthermore, three independently working heating elements were calibrated, for an optimized control of the reaction conditions within the quartz-reactor. Lastly, an analytical module was installed for analyzing and providing crucial information about the gas atmosphere within the reaction chamber (SO_3/SO_2 Determination, EPA-Method 8). In order to evaluate the functionality and reliability of CORA, IN718 and austenitic steel, as well as $Ti_{0.51}Al_{0.49}N$ and $Cr_{0.9}Si_{0.1}$ PVD coated austenitic steel substrates were tested. At an atmosphere of 1000 ppm SO_2, an oxygen equivalence of 150:1 and a flow rate of 1 m/min inside the quartz-reactor, the samples were corroded for 1 hour at 650°C and 850°C. In order to evaluate the aggressive salt induced corrosion effect, all experiments included both, samples with $Na_2SO_4/NaCl$ (30/70 mol.%) deposits, and without salt deposits.

In order to investigate the corrosive attack, analytical methods, such as XRD (X-ray diffraction), SEM (scanning electron microscopy) and EDS (energy dispersive X-ray spectroscopy) were utilized. Results showed that none of the material systems exhibited noticeable corrosion resistance for test conditions involving the salt slag deposits at HTHC (850°C). All experiments featured accelerated deterioration of the surface (involving coating as well as bulk), where porous oxide scale development and metal sulfide formation was observed. For corrosion experiments involving salt deposits at LTHC conditions (650°C), only the $Ti_{0.51}Al_{0.49}N$ and $Cr_{0.9}Si_{0.1}$ coatings showed superior corrosion behavior, while the uncoated IN718 and austenite samples continued to feature devastating deterioration. For tests in absence of $Na_2SO_4/NaCl$ deposits, all samples of interest exhibited substantial protection against the SO_x-rich atmosphere. In the case of IN718, formations of chromium oxide scales and mixed iron-nickel oxides provided good protection and significantly slowed down further oxidation of the material below. For austenite, a combination of iron oxide, iron-chromium oxide and manganese oxide also proved effective in hampering further oxidation in SO_x rich atmospheres, however a slightly inferior protective behavior compared to IN718 was noticed. In summary, CORA has shown to be an effective tool in providing highly aggressive HC conditions on a laboratory scale. Moreover, CORA has provided valuable first insights to the overall potential of PVD protective coatings as a strategic approach against hot corrosion.

Kurzfassung

In dieser Arbeit wird die Konzeptionierung und der Aufbau einer Heißgaskorrosionsanlage beschrieben. Das Konzept der Anlage wird von Grund auf dargestellt und alle wesentlichen Designkriterien erklärt. Heißgaskorrosion spielt in vielen technischen Anwendungen eine große Rolle, welche oftmals mit erheblichen Kosten verbunden sind. Der Korrosionsprozess wird durch SO_3 und Salzablagerungen an den Oberflächen der belasteten Komponenten vorangetrieben. Hohes Resistenzvermögen gegen diesen korrosiven Angriff wird PVD-Beschichtungen (Physical Vapor Deposition) zugesprochen. Um diese Beschichtungen im kleinen Maßstab testen zu können, wird ein Prüfstand, der reale Bedingungen emulieren kann, benötigt.

Für den Korrosionsprozess notwendige Gase wie Sauerstoff (O_2) und Schwefeldioxid (SO_2) werden mittels Massenflussregler justiert und einem zylindrischen Strömungsofen aus Quarzglas zugeführt. Als Trägergas wird Argon verwendet, welches ebenfalls reguliert werden kann. Im Ofen wird mittels eines Fe_2O_3-Katalysators die Oxidation von SO_2 zu Schwefeltrioxid (SO_3) vorangetrieben. Eine Salzmischung aus Natriumsulfat und Natriumchlorid wird auf die zu korrodierende Substratfläche aufgebracht, welche im Korrosionsprozess mit der SO_3 haltigen Atmosphäre reagieren. Um den Gehalt an SO_3 in der Atmosphäre zu bestimmen, wurde eine Abgasanalyse mit verschiedenen Gaswäschern nach dem Ofen eingegliedert. Nach den einzelnen Tests wurden die Flüssigkeiten in den Wäschern mittels einer Barium-Thorin-Titration analysiert.

Bei diversen Korrosionstests an unbeschichteten, sowie beschichteten Proben wurden die Testparameter so optimiert, dass Heißgaskorrosion an Turbinenkomponenten widergespiegelt wird. Ziel dieser Arbeit ist es nicht, die perfekte Beschichtung gegen Heißgaskorrosion zu finden, sondern zu zeigen, dass diese Korrosionsform auch im Labormaßstab abbildbar ist. Erste Versuche wurden an Proben aus INCONEL 718 und austenitischen Stahl, ebenso wie Beschichtungen aus $Ti_{0.51}Al_{0.49}N$ und $Cr_{0.9}Si_{0.1}$ auf austenitischem Stahl bei 650°C und 850°C für eine Stunde bei einem Sauerstoff-SO_2-Verhältnis von 150:1 durchgeführt. Um die Ergebnisse aus den Korrosionstests mit korrodierten Komponenten aus Industrieanlagen vergleichen zu können, wurden diese mittels XRD (X-ray diffraction), SEM (scanning electron

microscope) und EDS (energy dispersive X-ray spectroscopy) im Detail untersucht.

Die beiden Beschichtungen $Ti_{0.51}Al_{0.49}N$ und $Cr_{0.9}Si_{0.1}$ zeigen, speziell bei 650°C, verbesserten Korrosionsschutz. Verglichen damit, haben die unbeschichteten Substrate keine Beständigkeit gegen Heißgaskorrosion in Anwesenheit von Salzen und der Angriff große Teile des Substrates zerstört hat. Bei höheren Temperaturen (850°C) können die Schichten dem Korrosionsangriff nicht mehr widerstehen, was zu einem Angriff der Grundmaterialien führt. Dies wird vor allem dadurch bestätigt, dass sich ähnliche Testergebnisse bei unbeschichteten und beschichteten Proben einstellen und kaum Bestandteile der Schichten in der Analyse nachgewiesen werden können. Es bilden sich poröse Korrosionsprodukte, welche aus komplexen Metalloxiden- und -sulfiden bestehen und sich an den Oberflächen ablagern. Zusätzlich dazu kommt es zu Oxidation und Sulfidierung bis tief ins Material hinein.

Die zuvor beschriebenen Korrosionsmerkmale können ebenfalls bei Industrieanlagen beobachtet werden. Die konstruierte Heißgaskorrosionsanlage ermöglicht daher eine effiziente Erprobung von diversen Materialien im Labormaßstab und legt den Grundstein für die Weiterentwicklung von PVD-Schichtsystemen in Hochtemperaturanwendungen.

Chapter 1

Introduction

The development of superior materials and components, used within the energy and transportation sectors, is an indispensable asset to any industry eager to push the frontiers in technology. In this regard, improved material properties are the key for better machining performance, efficient service times, as well as an extended lifetime of costly components [1].

Particularly in high temperature regimes such as gas turbines, accelerated degradation of material surfaces pose a substantial problem to the engines performance, and forces companies to conduct more frequent maintenance. Whereas oxidation of materials at higher temperatures is a well-understood phenomenon in gas turbine systems, a more aggressive degradation of the turbine components occurs due to a corrosive process called hot corrosion (HC) [2]. Sodium chloride (NaCl) rich aerosols from marine environments enter the combustion chamber, react with oxygen (O_2) from the air intake and sulfur (S) impurities from the fuel, and form sodium sulfate deposits (Na_2SO_4) [3].

Unlike a pure oxidation, where air from the intake and hot exhaust gases react with the metal surfaces to form protective oxide scales, HC takes place when salt particles come into direct contact with turbine components and promote accelerated surface reactions that rapidly diminish the integrity of the material. Once the salts have deposited on the turbine hardware, the corrosion mechanism depends significantly on whether the Na_2SO_4 deposits are fused as a solid aggregate or adhere in a molten state. The fundamental corrosion mechanism is thus substantially dictated by the temperature regime of the turbine environment. If the temperature of the turbine environment exceeds the melting point of the adhered salts, the corrosion mechanism is referred to as Type I high-temperature hot corrosion (HTHC). If the temperature environment remains below the melting point of the salt deposit, the mechanism is called Type II low-temperature hot corrosion (LTHC). The accurate reactions depend on the material system, the composition of the surrounding atmosphere and the chemical make-up of the salt deposits. Therefore, a prediction of the specific reaction mechanisms of material systems and their environment become quite difficult [4, 5]

INCONEL, a nickel-based superalloy family, is widely used in high-temperature applications, due to their excellent mechanical properties at high temperature, their oxidation resistance, their elevated thermal stability and their good workability [2]. Especially in aircraft and land-based gas turbines, INCONEL is used as structural material for highly stressed parts up to high temperatures [6]. At critical limits of molten salts and sulfur in the atmosphere, INCONEL shows insufficient resistance against hot corrosion, which leads to degradation of the material. Further research in hot corrosion resistant of materials is consequently inevitable [7]. The development of new protective materials is not easy, because beside a good resistance against hot corrosion, other important properties like oxidation resistance and high temperature strength has to be fulfilled inside gas turbines [1].

A combination of the needed properties can be provided by coating systems on top of the components. The coating protects the material from the environment and on the other hand, the needed bulk material properties are unchanged. Therefore, a high potential is credited to various coating techniques. The development of these coating is ongoing and first high-temperature components are protected with coatings, but the full potential is not arrived yet. The most-used concepts are thermal barrier coatings (TBC), where a thermal insulation layer on top of the surface preserves the material against high-temperature failures. Typically, a metallic interlayer is also applied, which is reliable for excellent oxidation resistance and proper adhesion between bulk material and TBC [1]. Yttria stabilized Zirconia TBC are frequently used in high-temperature applications, whereas a MCrAlY (where M is Ni, Co or a combination of both) [8] or a platinum-modified nickel aluminide coating is applied as metallic interlayer [9]. This type of coatings meets the requirements for high-temperature applications in absence of salts. At hot corrosion conditions, the state-of-the-art TBC has marginal corrosion resistance, which leads to degradation of the coatings and so, the material beneath is unprotected [9]. The ceramic top coating is applied with electron beam physical vapor deposition (EB-PVD) or atmospheric plasma spraying (APS) [10].

The investigations of proper physical vapor deposition (PVD) coatings in hot corrosion conditions is pushed forward by their corrosive resistance potential [10]. The coating technique is developed in a wide range of applications, especially where high wear resistance and high working temperatures are needed. With this coating technique, different material systems can be deposited on various bulk materials and so, the inertness of the material result from the protective thin layer on top of a non-resistant material, whereas the mechanical properties depending on the substrate material. Resistance of widely used PVD-coatings with ceramic characteristic against hot corrosion should be investigated in more detail, but the potential of protective thin films in harsh environments is unquestioned [11]. New concepts of PVD coated components in hot corrosion ambient will be investigated with different characteristics of the material systems.

The aim of the thesis was the development of a concept for testing various materials against hot corrosion. The focus of the testing rig is to investigate the resistance of different coating systems at gas engine conditions. The concept is coordinated with a built-up inside a fume hood, whereas the safety measures in laboratories are complied. To observe the hot corrosion mechanism and its limiting characteristics, the configurability of gas compositions inside the testing chamber is realized. Research of both hot corrosion forms (LTHC and HTHC) are achieved by a furnace system with accurate substrate temperature measurements up to 1100°C. The testing rig was mechanical constructed according to the developed concept. Austenitic steel and INCONEL 718, as well as $Ti_{0.51}Al_{0.49}N$- and $Cr_{0.9}Si_{0.1}$-coated austenite were tested and analysed for reproduction of the hot corrosion mechanism inside the construction.

CHAPTER 2

Theoretical Background

2.1 Corrosion Mechanisms

Corrosion defines the chemical interaction between a material and its respective environment over a period of time. Often, only the aspect of degradation is considered (a case of corrosion where environmental influences drastically diminish a materials properties and thus, reduces its technical reliability) as corrosion, whereas to include corrosive processes that merely elicit a chemical transformation of a material without diminishing its technical integrity is equally appropriate. In the latter case, this is often observed for metallic materials, where a reaction between the metal surface and its surrounding produce a metal oxide layer, which in many cases can function as a barrier for further reactions between metal and environment. This beneficial barrier, also called passive layer, can be viewed as a limited corrosion reaction, which results in the formation of a rate controlling corrosion product. Therefore, corrosion is not always an unwanted occurrence, but a sough after event if it aids the preservation of material components. Therefore, corrosion and corrosion-resistance are essential variables, that if properly understood, present an indispensable tool for designing high-performance components [12].

Every chemical reaction needs a driving force. For example, for metals and the formation of their respective oxides, thermodynamic and kinetic criteria have to be considered. Whereas thermodynamics merely describes the energetically feasibility of a chemical reaction (Gibbs free energy criterion), the kinetic aspect describes the rate at which a reaction progresses (reaction rate-constant). Together, they allow material scientists and engineers to predict, under which circumstances and environmental conditions a surface metal-oxide layer can form. In other words, oxidation, or in fact any corrosion reaction will occur, if the change in Gibbs free energy is < 0 and conversely, will not occur if the change in Gibbs free energy is > 0 [13, 14].

The definition of the difference in Gibbs free energy between two states inside a system is given in Equation 2.1

$$\Delta G = \Delta H - T \cdot \Delta S \tag{2.1}$$

,where Δ G is the change in Gibbs free energy, Δ H the change in enthalpy, T the temperature and Δ S the change in entropy. Enthalpy is characteristic for the energy state of the system. The change in enthalpy occurs whether energy is absorbed from the environment (endotherm reaction), so Δ H is positive or energy is released to the environment (exotherm reaction), where Δ H is negative. Entropy refers to the capacity for spontaneous change inside the system, whereas the proceeding reaction decreases the level of order inside the system for positive values of Δ S [12].

There are many different forms of corrosion, which have their own mechanism. A classification of the corrosion mechanisms should be made, where the processes are sorted to their properties. The easiest classification is made by their environmental influences and their damage appearance, as given in the following chapters.

2.1.1 Corrosion Systems Defined by Environmental Influences

The environment of the material plays a decisive role in the corrosion process. An overview of the most important media is given in Figure 2.1. The mechanism of each corrosion type varies with the different outer influences, which will be discussed hereafter.

Corrosion types according to outer influences can be classified as:

- Corrosion in aqueous media
- Corrosion in dry Gases and vapors
- Corrosion in salt and liquid metals, in absence of aqueous media
- Mechanical assisted corrosion

Corrosion can occur for a variety of reasons and the whole system must always be considered to fully understand the corrosive mechanism.

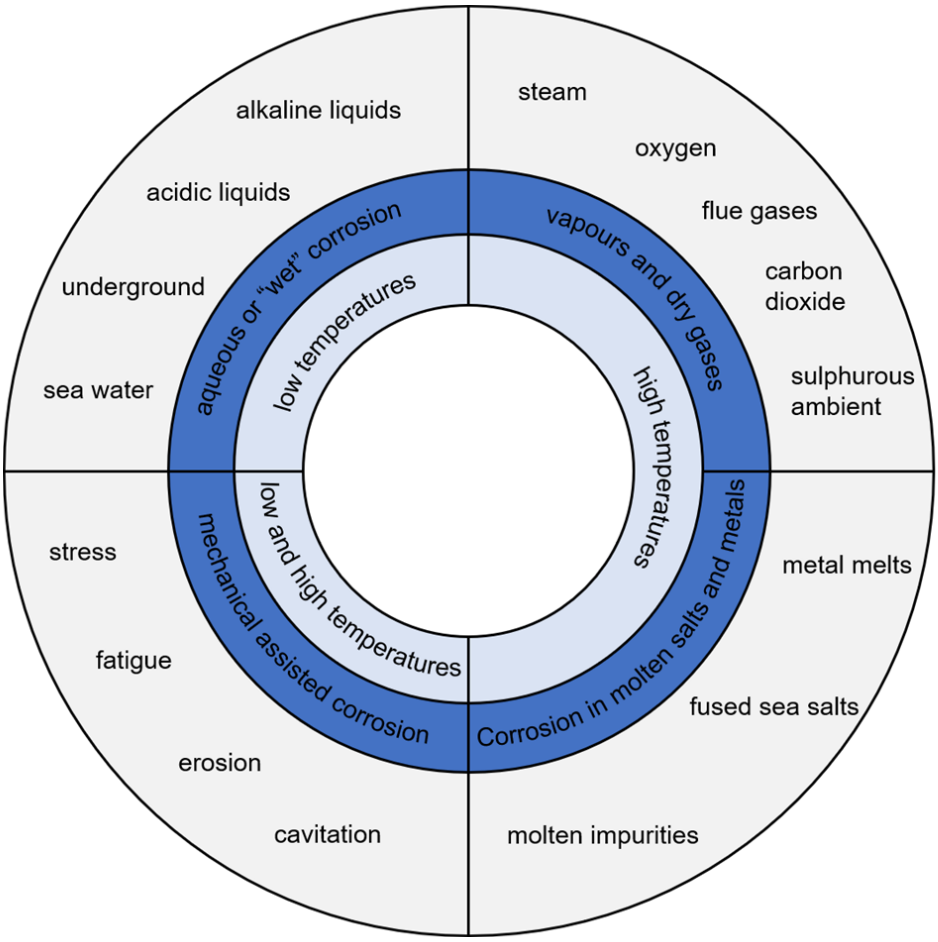

Fig. 2.1: Classification of environmental influences in corrosion systems, adapted from [12].

Aqueous Corrosion

This corrosion type is based on electrochemical reactions between parts of the material surface and an electrolyte. Two electrochemical half-reactions, called anodic and cathodic reaction, occur on different places, which is responsible for the corrosive attack. In the presence of an aqueous media, the different partial reactions exchange electrons with each other. The requirement for this mechanism is electrical conductivity of the material and ionic mobility within the solution in contact with the material surface, forming a redox-couple and functioning as a galvanic cell. At the cathode, the reduction of the electrolyte occurs with the consumption of electrons. The needed electrons for the cathodic reaction, in turn, come from the anode, where the dissolution of metal occurs and electrons are liberated. Between an anodic and a cathodic reaction, an electric potential is formed due to the chemical potential of each half-reaction with respect to the electrolyte and overall conditions of the system (pressure, activity, temperature). A prediction of the occurring reactions can be given by the electrochemical series. Standard electrode potentials provide knowledge, which species will partake as a reducing agent and which species will engage as an oxidizing agent. In 2.1, a few examples of the electrochemical series are prepared, whereas the standard electrode potentials result from reactions under standard conditions (1 atm, activity of 1 and 25°C), whose electrochemical potentials have been measured using a standard hydrogen electrode.

Table 2.1: Electrochemical standard potential for exemplary reactions.

oxidized form ↔ reduced form	standard potential [V]
$Cl_2+2e^- \leftrightarrow 2Cl^-$	+1.36
$O_2+4H^++4e^- \leftrightarrow 2H_2O$	+1.23
$Cu^{2+}+2e^- \leftrightarrow Cu$	+0.34
$2H^++2e^- \leftrightarrow H_2$	0
$Fe^{2+}+2e^- \leftrightarrow Fe$	-0.41
$Cr^{2+}+2e^- \leftrightarrow Cr$	-0.91
$Al^{3+}+3e^- \leftrightarrow Al$	-1.66

To clarify the electrochemical mechanism in more detail, the reactions are presented with the example of iron corroding in presence of a water droplet. The circumstances of the corrosive process are illustrated in Figure 2.2. Iron atoms liberate electrons to the cathodic reaction and dissolve as metal anions into the water droplet.

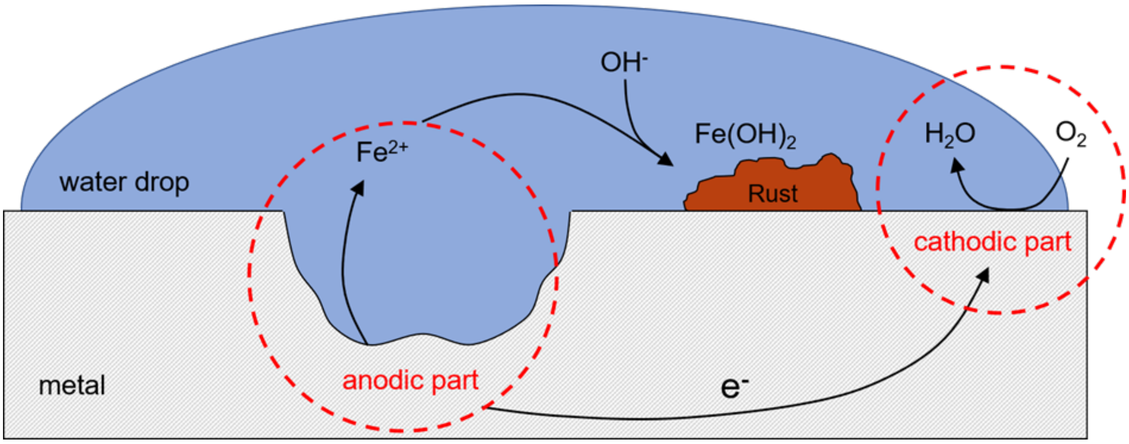

Fig. 2.2: Aqueous corrosion of iron in presence of a water droplet, adapted from [15].

At the cathodic site, oxygen is reduced, whereas the mechanism depends on the overall pH of the media, which can be compared with Equation 2.2.

$$\begin{aligned}
Anodic\ half - reaction :&= 2Fe \rightarrow 2Fe^{2+} + 4e^{-} \\
Cathodic\ half - reactions :&= O_2 + H_2O + 4e^{-} \rightarrow 4OH^{-} \quad (for\ neutral\ or\ basic\ solutions) \\
&= O_2 + 4H^{+} + 4e^{-} \rightarrow H_2O \quad (for\ acidic\ solutions) \\
\hline
Complete\ RedOx - reaction :&= 2Fe + O_2 + H_2O + 4e^{-} \rightarrow 2Fe^{2+} + 4OH^{-} \rightarrow 2Fe(OH)_2
\end{aligned} \tag{2.2}$$

The metal anions react with the OH^{-} ions and precipitate as $Fe(OH)_2$ on the surface, which is also called rust. The water drop serves as the electrolyte, which transport the metal ions to sections of precipitations [13, 14].

Mechanical Assisted Corrosion

One of the most common forms of mechanical assisted corrosion types are stress corrosion cracking (SCC) and corrosion fatigue cracking (CFC). These forms of corrosion rely on a combination of mechanical stresses and reactive media. The reactive environment can lower the materials tensile strength and fatigue strength, which leads to a component failure below critical loads. The material stresses, which lead to SCC, can not only originate from applied static forces, but also residual forces from heat treatment, welding, cold work, etc. In contrast, the CFC is caused by dynamic forces, so this type is based solely on outer influences.

The corrosive products accumulate in the crack tip and the media inside the crack changes in concentration. Therefore, the corrosive attack is changing during the process, which accelerate the corrosion in worst cases. Based on the corrosive mechanism, the cracks can either move along grain boundaries (intergranular) or traverse the grains (transgranular) [16–18].

High-Temperature Corrosion (HTC)

At elevated temperatures, aqueous solution begins to evaporate and aqueous corrosion becomes less likely. Instead the material surfaces may still undergo chemical changes within their given environments. The mechanism of the corrosive process at high temperatures depends on the nature of the environment, taking the presence of molten salts in especial account.

HTC in Dry Environments – For high-temperature condition with absence of an electrolyte, the environment interacts directly with the surface. The most important reaction is the oxidation of metals. The oxidation creates a valence state of the metal, which is higher than the metallic state and thus, is the driving force for the reaction. Depending on the material and the ambient conditions, the oxide can be protective or not. The most important parameters for defining the oxides are temperature and oxygen partial pressure. The most basic part reactions, that happen during oxidation are given below:

$$\begin{array}{r}
Oxidation\ of\ the\ metal := Me \rightarrow M^{2+} + 2e^{-} \\
Reduction\ of\ oxygen := \frac{1}{2}O_2 + 2e^{-} \rightarrow O^{2-} \\
\hline
Metal - oxide\ formation := Me + \frac{1}{2}O_2 \rightarrow MeO
\end{array} \tag{2.3}$$

There are other forms of surface reaction with hot gases. Beside oxidation, sulfidation, carburization and nitriding are the most occurring high-temperature processes. The reaction between gaseous phases and material surfaces can be hazardous, but in many applications also desired [8, 19]. For example, oxidation of nickel-base superalloys at controlled conditions promote an immaculate Cr_2O_3 or Al_2O_3 (depending on the composition of the material) protective layer, which enhance the resistance against hot corrosion [2].

HTC with Salt Slag Deposits – The corrosion rate in high-temperature systems increase rapidly in the presence of salt deposits between 600°C to 950°C. These salts interact as media on the surface in the reaction system and inter alia, electrochemical reactions affect the material. Either they interact with the surface and inhibit the development of a protective oxide layer, or they react with the oxide to porous non-protective layers. Halides, nitrates, sulfates and carbonates are the most critical salts for corrosion in technical applications [8]. Destruction of components due to hot corrosion is mainly seen in energy systems like gas turbines and jet engines.

Hot corrosion occurs at temperatures between 600°C and 950°C, where salt rich aerosols from marine environments react with impurities from the fossil fuels and form highly corrosive salt deposits. Depending on the aggregate of salt deposit that forms in contact with the turbine component surfaces, two types of hot corrosion can be differentiated:

- High temperature hot corrosion type I (HTHC) ~750°C to 950°C
- Low temperature hot corrosion type II (LTHC) ~600°C to 850°C

The dividing line of the two mechanism is defined in many ways, but the most accurate one is the melting point of the salt deposit. Below the melting point, LTHC occurs, whereas at higher temperatures, the HTHC mechanism takes place. The severity of hot corrosion is illustrated in Figure 2.3, where the severity of the corrosive attack is compared between LTHC, HTHC and pure oxidation. The exact process of both types will be discussed in chapter 2.2 [4, 7, 8].

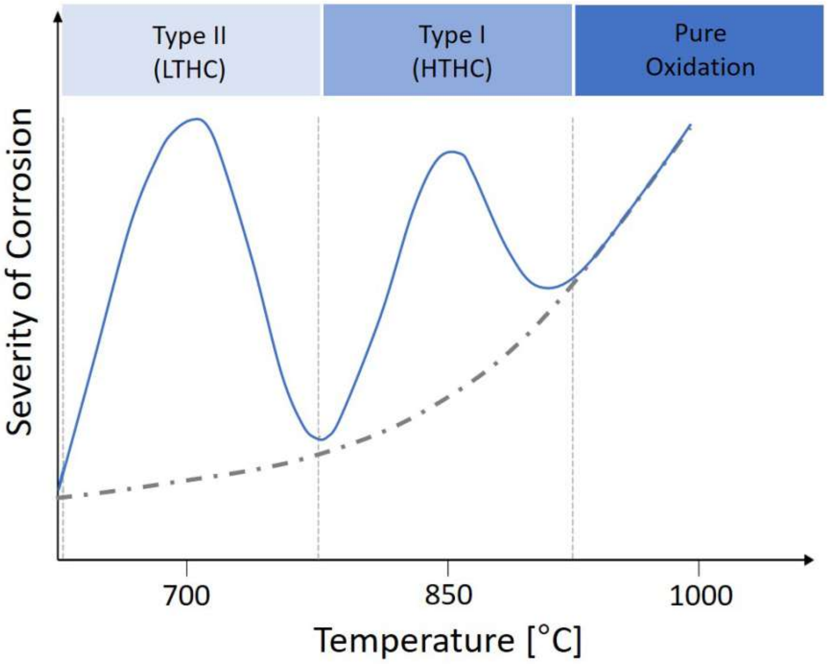

Fig. 2.3: Severity of corrosion at elevated temperatures with hot corrosion mechanism (solid line) and without hot corrosion mechanism (dashed line), adapted from [20].

2.1.2 Corrosion Systems Defined by their Damage Appearances

Throughout this section, an overview of the various corrosion appearances will be provided in more detail. Contrary to Section 2.1.1, where the categorization of corrosion types was discussed according to their respective environments, corrosion processes may equally be classified by their physical appearance.

Uniform Surface Corrosion

Probably the most common corrosion process is the uniform surface corrosion. All areas of a material corrode at the same (or similar) rates, which can be predicted fairly well. Components get thinner and the surface is roughened in many cases, which leads to a deterioration of mechanical properties.The most common examples are oxidation and tarnishing of metal surfaces, active dissolution in acids and anodic oxidation and passivation of metals [13, 18]. Also, hot corrosion Type I can appear in an uniform damage and therefore, gas engines in temperature areas between 750°C and 950°C can be corroded with this type of damage [4].

Pitting

Pitting corrosion describes a form of a highly localized attack at specific areas, resulting in the formation of small cavities or holes. Pit initiation may occur at effect sites, pinholes, or scratches in a protective film, or along inclusions or grain boundaries near the surface. Once a small pit has formed and direct contact between the corrosive medium and the bare metal exists, an accelerated and self-sustaining pit-propagation ensues. The very small, localized anode (dissolution of metal into the electrolyte) – compared to the cathode (consumption of electrons via reduction of the oxidizing agent) – leads to a fast corrosion process toward the middle of the component, which is illustrated in Figure 2.4a. Due to the very small cracks or cavities that form during pit initiation, and a near to undetectable pit growth below the surface, pitting is regarded as the most dangerous and insidious type of corrosion.

Pitting corrosion occurs in different ways. The size of the anode and cathode is the most important factor, but also the transport of the corrosion products to the surface can vary throughout pitting mechanisms. For larger anodes, the attack will be wider and near to the surface, seen in Figure 2.4b. Frequently, the corrosive process is originated on a small defect inside the protective layer and the aggressive media is transported through this small area to the bare, unprotected material, whereas an attack is continued beneath the surface in wide areas with material depending preferred degradation routes, given in Figure 2.4 c-f [13, 17].

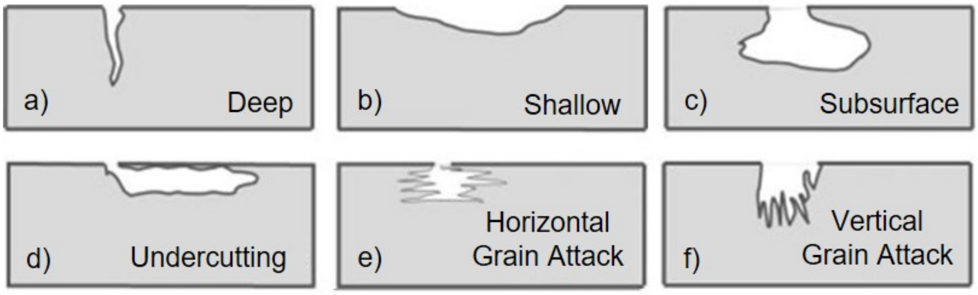

Fig. 2.4: Different forms of pitting corrosion, adapted from [21].

In LTHC, pitting corrosion is the dominating degradation form of the material. The oxide layer is attacked locally due to a non-uniform protective layer and so, the aggressive media attack the metal beneath at these defects. Especially in nickel-base superalloys with imperfect Al_2O_3 protective layers, the corrosive process enforced at nickel or cobalt oxide formations inside the surface film and afterwards, these areas cannot be regenerated by a protective film because of the ambient sulfuric media [2].

Intergranular Corrosion

For intergranular corrosion, a preferred attack of the material occurs at the grain boundaries. The cohesion between grains is downgraded by a localized attack, which leads to a separation of the material along the grain boundaries. In many systems, reactive impurity segregation or composition differences at grain boundaries, cause a higher susceptibility of the material at these regions. The formed corrosive product extent at the grain boundaries imply mechanical stresses, which lead to a decrease in decisive mechanical properties [16, 18]. A typical form of intergranular corrosion through brass is illustrated in Figure 2.5, where the preferred corrosion path leads on the grain boundaries through the material, due to dezincification at these areas [13].

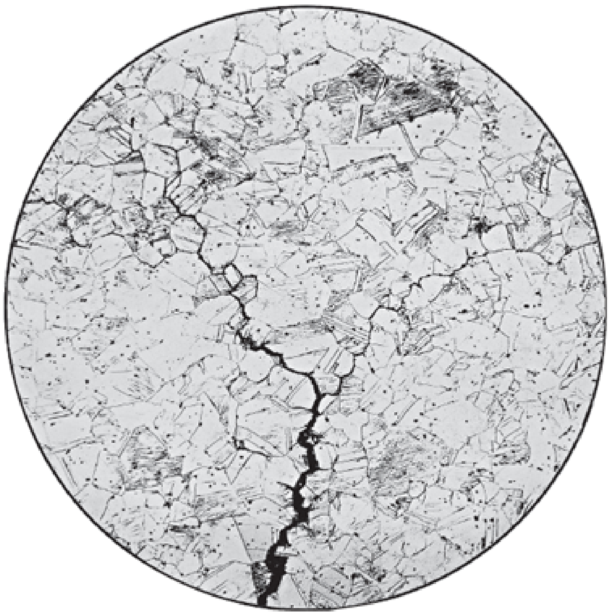

Fig. 2.5: Typical profile of intergranular corrosion in brass, analysed under an optical microscope [13].

Intergranular corrosion can be activated by high temperature conditions. For example, at sulfur-bearing gaseous environment, nickel-base superalloys form low melting point nickel sulfides. This sulfidation process penetrates the grain boundaries and lead to catastrophic material failures [13].

Selective Corrosion (Dealloying)

Selective corrosion is the depletion of a specific element inside a material. The area, which is most prone to this type of corrosion, has a significant different elemental composition, which leads to a potential difference inside the material. This potential difference drives a dissolving reaction forward and damage the component. Usually, the substrates stay in the same shape and the surface is not changed very much, but the material properties like tensile strength, fracture toughness and resistance to fatigue will worsen significantly. For example, cast iron corrode frequently in underwater pipe systems. The ferritic and pearlitic phase dissolves due to potential difference to the graphite and cementite phases. This process is called spongiosis, due to their spongy appearance form after the corrosive impact [13, 18].

Selective corrosion has also a high impact on HTHC, whereas after sulfidation of specific alloy elements, a selective oxidation of the formed metal sulfides succeeds. The corrosive attack is accelerated, due to the released sulfur, which continue the sulfidation in inner parts of the material. The oxidation/sulfidation mechanism leads to catastrophic damage inside the material, which is also seen in Figure 2.6 [2].

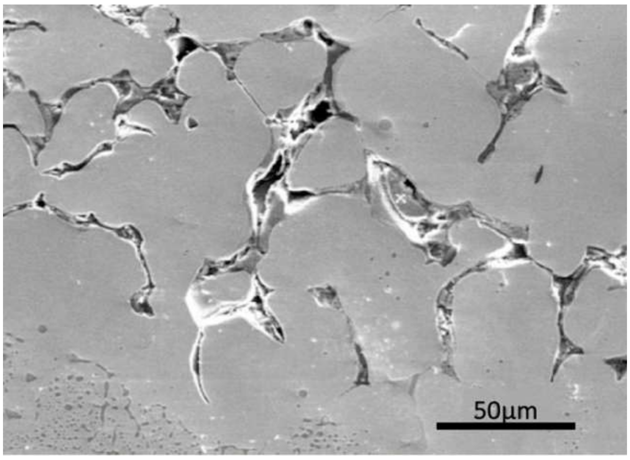

Fig. 2.6: Sulfidation of nickel inside a nickel-base alloy in HTHC conditions at 900°C. The liquid state nickel sulfides (dark parts) are transformed in oxidized state and the corrosive process continues [22].

2.2 Hot Corrosion

An overview of different corrosive mechanisms and their appearances are described in previous chapters. The primary corrosion process in this thesis is described by the hot corrosion and so, this form of corrosion should be highlighted more precise.

In many technical applications at elevated temperatures, hot corrosion is responsible for an accelerated degradation of materials, leading to catastrophic failures in machining components. The thermal stability of many materials would be sufficient, but with salts inside the atmosphere, the corrosive severity increases drastically. In the case of gas turbines and jet-engines, sulfur impurities in the engine fuel reacts with oxygen inside the combustion chamber. This undesired oxidation leads to formations of SO_2 and SO_3 [4]. On the other side, the intake air consists of many different salts, especially in sea water regions. These salts are not very harmful but react with sulfur and oxygen to corrosive salts. The most dangerous reaction for hot corrosion is based on the presence of NaCl. SO_2 and SO_3 react with the salt, which leads to formations of Na_2SO_4 [23, 24]. The stepwise reactions to form the aggressive media are presented in Equation 2.4 [2].

$$\begin{gathered} S_2 + 2O_2 \rightarrow 2SO_2 \\ 2SO_2 + O_2 \rightarrow 2SO_3 \\ NaCl + SO_3 + H_2O \rightarrow Na_2SO_4 + 2HCl \end{gathered} \tag{2.4}$$

The mixture of salts can adhere on component surfaces and is transformed there to liquid state, which serves as the corrosive media. The gas phase and the metal surface are separated by the salt film. In open circuit systems with combustion installations, the supply of salts and sulfur is continuous. As long the mixture can participate on the reaction, the corrosive attack is sustained [12]. The molten Na_2SO_4 dissolves partially in NaO_2 and SO_3, given in the following equilibrium Equation 2.5 [23].

$$Na_2SO_4 \leftrightarrow Na_2O + SO_3 \tag{2.5}$$

The content ratio between Na_2O and SO_3 inside the melt defines the basicity character, whereas the contents of both species are indirect proportional to each other at determined amount of Na_2SO_4. The corrosive mechanism depends on the basicity of the melt, so the dissolving process is also called *acid/basic fluxing*. By reactions between the protective oxide layer and SO_3, positive charged metal ions Me^{n+} are produced and so, an electron acceptor species inside the melt is generated (which is defined as acidic solution). The principle mechanism of the so-called *acid fluxing* is presented by Equation 2.6, together with the generic chemical reaction for the acidic dissolution of nickel oxide [2, 4].

$$\begin{gathered} metal\ oxide + SO_3 \rightarrow Me^{2+} + SO_4^{2-} \rightarrow metal\ sulfate \\ NiO + SO_3 \rightarrow Ni^{2+} + SO_4^{2-} \rightarrow NiSO_4 \end{gathered} \tag{2.6}$$

At higher Na_2O content (respectively O^{2-} concentration) inside the molten salt deposit, another mechanism takes place. The oxygen ions react with the oxidic surface layer to metal-oxyanions, serving as an electron donator, synonymous to the definition of a basic solution and thus, known as basic fluxing. The metal-oxyanions diffuse into the melt and the dissolving process initiates. The principle reaction of basic fluxing, as well as an examplary reaction for alumina is given by Equation 2.7 [2, 9].

$$\begin{gathered} metal\ oxide + O^{2-} \rightarrow metal\ oxyanion \\ Al_2O_3 + O^{2-} \rightarrow 2AlO_2^- \end{gathered} \tag{2.7}$$

The occurring mechanism (*acid or basic fluxing*) depends on the partial pressure of SO_3 (indirect proportional to the Na_2O content) inside the corrosion system. At determined SO_3 partial pressure, a transition zone between both mechanism is established with a minimum of dissolving oxide layer rate, given in Figure 2.7 as the minimum amount of metal ions concentration in Na_2SO_4. The determining SO_3 partial pressure for the transition zone varies with the metal oxide type [4, 23]. High contents of SO_3 comes from the oxidation of SO_2 and the combustion of fuel. On the other hand, high Na_2O concentration are generated by the presence of high NaCl contents, which can be oxidized and form sodium monoxide [4].

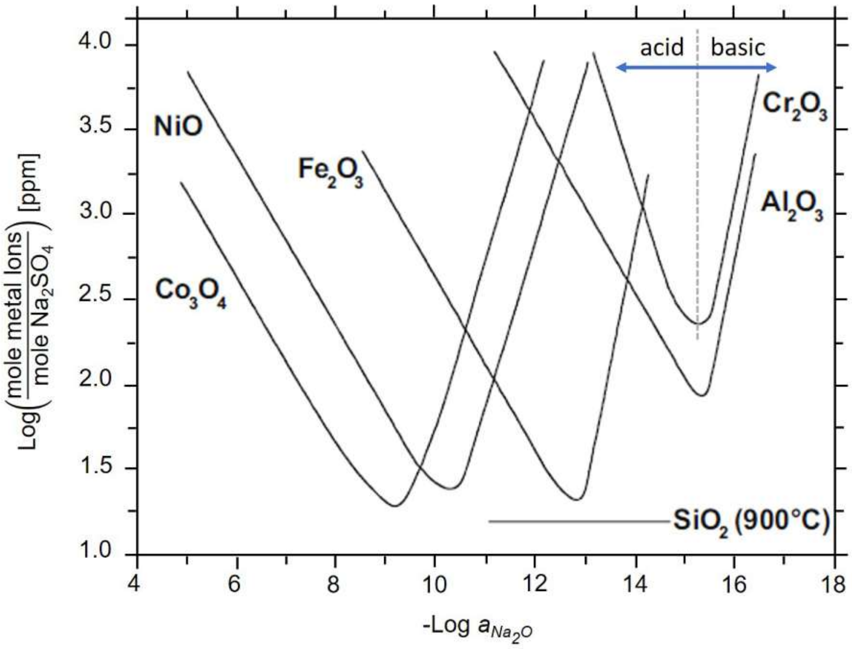

Fig. 2.7: Severity of different metal oxide degradation depending on the SO_3 partial pressure (expressed by the negative logarithm of Na_2O activity), adapted from [25].

The solubility gradient of oxides inside the molten deposits is responsible for the regenerative properties of the protective layers. The oxide dissolve in the molten salt by *acid/basic fluxing* and if the solubility is lowered with distance to the oxide-salt-interface, the oxide reprecipitate in outer regions as porous, non-protective oxide layer [23, 24]. The precipitation procedure of metal oxides is presented exemplary on acidic fluxing mechanism in Figure 2.8.For LTHC and HTHC, different corrosive mechanisms are characteristic, which are examined in the following chapters.

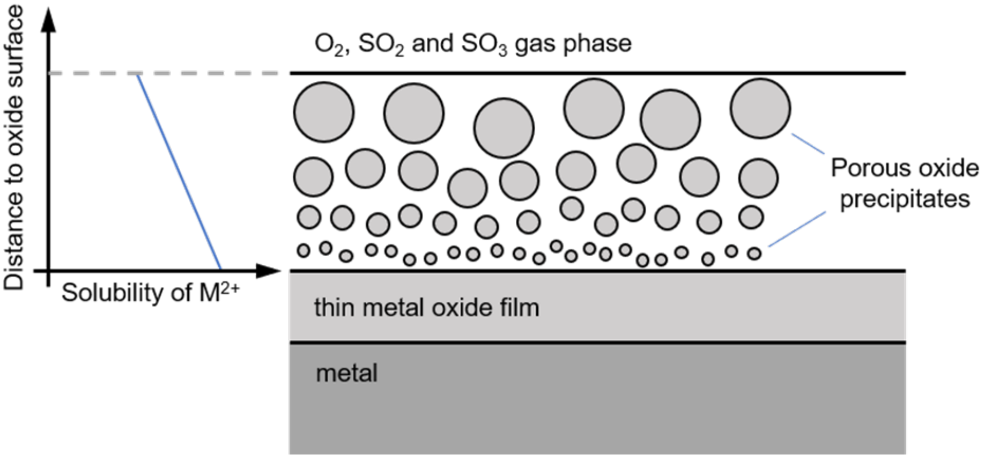

Fig. 2.8: Dissolving mechanism of protective oxide layers in acidic salt melts, adapted from [26].

2.2.1 Hot Corrosion Type I (HTHC)

The mechanism of HTHC relies on the liquid state of the salt slag deposits. A mixture of salts, for example Na_2SO_4 and NaCl, lower the salt melting temperature, due to the formation of a eutectic. The dissolving process of the oxide layers is enforced over the whole salt covered surface and without a protective layer, the corrosive process goes deep through the material. At high temperature levels, the oxidation rate of SO_3 is lowered (which will be analysed in chapter 2.3.2) and so, a basic fluxing mechanism is favored [2]. The dissolved oxide layer reprecipitate as porous, non-protective metal oxide formation at the salt-gas interface near regions. Without the protective layer on the surface, corrosive reactions inside the material takes place in form of sulfidation, whereas the diffusing sulfur is released by the melt. This diffusion procedure cannot be prevented by the oxide layer and so, the sulfidation continues [4, 23]. Slow diffusion of oxygen - compared to the diffusion rate of sulfur - inside the material leads to oxidation of the formed metal sulfides, whereas the released sulfur migrates toward the component center and so, sulfidation occurs again inner areas of the material. With this oxidation/sulfidation process, the corrosive attack is self-sustained. Without preventing measures, the HTHC leads to catastrophic failures in high-temperature applications [2].

2.2.2 Hot Corrosion Type II (LTHC)

A corrosion process occurs at lower temperatures of about 600°C to 850°C. At these temperatures, the salt mixtures are in solid state, but react with the material surface. First, metal oxides react with the salts and form low melting point solid complex. During LTHC conditions, this complex interlayer goes into a liquid state, for example a Na_2SO_4-$NiSO_4$ layer. The formation of the liquid layer drives the dissolution of the oxide forward and a porous oxide layer remains. [23]. Before the destructive process occur, an incubation period with the development of the complex liquid interlayer is needed in advance [24].

The presence of SO_3 is mandatory for LTHC because the sulfur trioxide participate in the chemical reaction between salt and oxide precipitations and so, LTHC is referred to acid fluxing [2]. The partial pressure of SO_3 in the environment of the substrate is determinant for the dissolution of the oxide layer and so the corrosion process is stopped at lower limits. The attack is localized on imperfections of the protective oxide layer. For example, uniform Cr_2O_3 surface layers on nickel-base superalloys cannot be affected at typical SO_3 partial pressure, whereas nickel oxide parts in the outer layer are attacked locally. After destructing the layer at these areas, the corrosion continues in wider areas beneath the surface layer. Therefore, LTHC leaves a damage pattern which is linked up with localized pits. The destructing process is enforced only on surface near regions, throughout no significant inner sulfidation affect the material [2, 24].

2.3 Conceptualization of Hot Corrosion Testing Rig

2.3.1 Configuration of the Testing Atmosphere

In hot corrosion, the content of SO_3 is one key characteristic for the corrosive attack. The formation of SO_3 needs sulfur and oxygen, so the source and content of these components should be considered. A very important intermediate reaction is the formation of SO_2, and its subsequent oxidation to SO_3. Therefore, the content of SO_2 and SO_3 should also be discussed.

Impurities of sulfur inside the fuel leads to formations of SO_2 and SO_3 during the combustion process. The content of sulfur inside diesel fuels and petrol is approximately 0.5 wt.% [27]. Inside the combustion chamber, the oxidation of sulfur is favored to form SO_2 instead of SO_3, whereas the amount of SO_3 should be much higher thermodynamically. The residual time inside the burning process is very short, whereas the kinetic conversion rate of SO_2 to SO_3 is low at temperatures below 900°C (compared to Figure 2.9) and so, the content of formed SO_3 in the combustion process is negligible. The elevated concentration of SO_3 inside the system are formed from oxidation of SO_2 after the combustion process. The quantity of SO_x

conversion from sulfur is in aircraft engines about 3 wt.% to 10 wt.% referred to the total sulfur content.

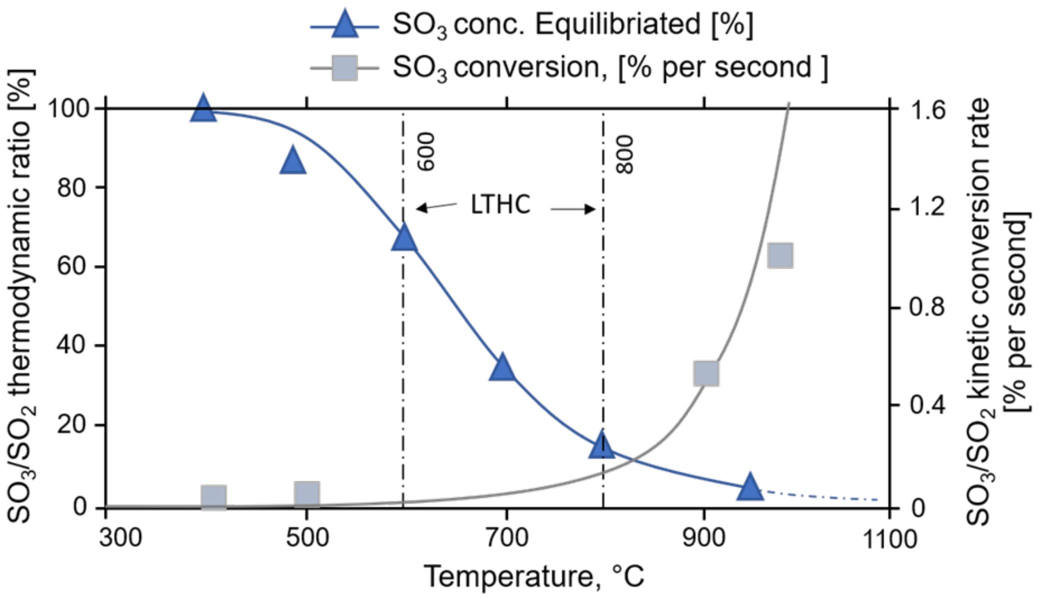

Fig. 2.9: Thermodynamics and kinetics of SO_3/SO_2 conversion varied with temperature, adapted from [28] and [29].

The conversion of SO_2 to SO_3 is influenced by many factors. The partial pressure of O_2 and SO_2 inside the gas flow is decisive, but also the presence of a catalyst is very important.

The relationship between the partial pressure of oxygen and SO_2 has a high impact for the SO_3 transformation. In combustion chambers, the level of this relation is depending on the air-fuel ratio λ, whereas the SO_3 concentration rises with higher air content. This fact is confirmed in Figure 2.10, where the conversion of SO_3 rises with the concentration of oxygen compared to the fuel quantity [30].

The ratios of air-to-fuel can vary by the engine type, so a wide spectrum should be covered. Typical air-to-fuel ratios are between 1:1 and 15:1. To transform the air to fuel ratio in oxygen to sulfur dioxide ratio, both contents should be analyzed. Starting from a 5 wt.% SO_2 content inside the fuel and 23.3 wt.% O_2 inside air, a ratio between 4:1 and 60:1 between O_2 and SO_2 in the testing rig is necessary.

The very slow conversion rate of SO_2 to SO_3 is accelerated in presence of catalysts. Fly ash, which is formed during combustion, has activator-particles inside and therefore are promoting for the conversion of SO_2 to noticeable SO_3 amounts. For example, Fe_2O_3 within the ash particles, serve as a very good accelerator of the reaction. The conversion rate of SO_3/SO_2 rate can be improved by an order of magnitude [31]. For the construction of a testing rig, flying particles always cause problems with the cleanliness of the system. Therefore, a solid catalyst, which cannot be carried away with the gas flow, is optimal for the test runs.

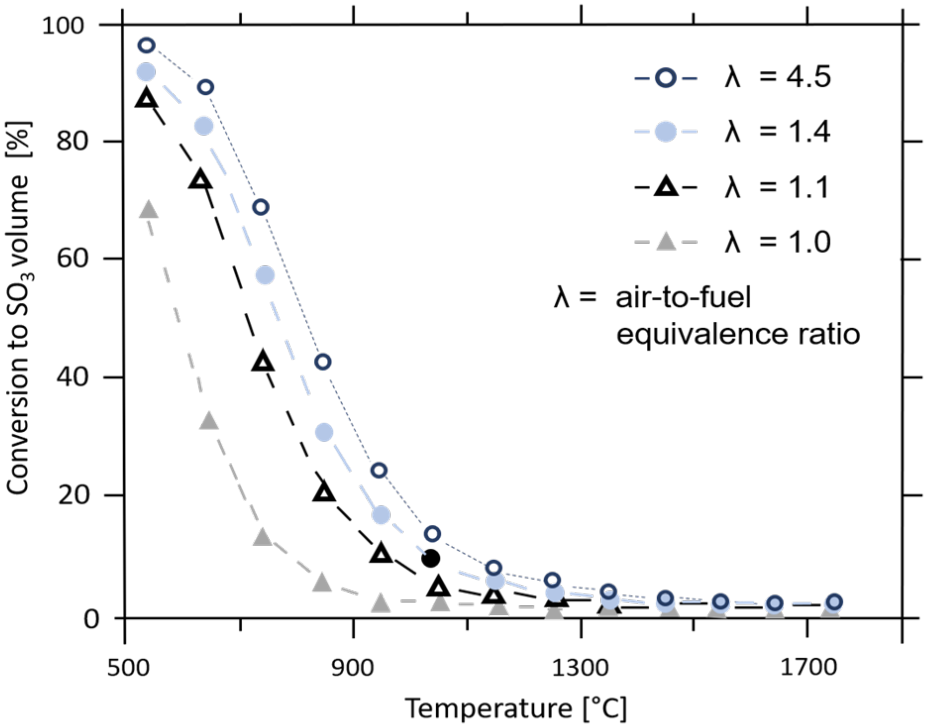

Fig. 2.10: Change in SO_3 transformation for different fuel-air ratios, adapted from [30].

2.3.2 Theoretical Basics for Heating Concept

The heating concept of the testing rig is one of the most important parts of the performance of the testing rig. First, the optimum temperature for the catalytic effect for SO_2 oxidation should be discussed, based on the background of chapter 2.3.1. A change in temperature has two counteracting mechanism for the SO_3/SO_2 conversion:

- The thermodynamic equilibrium is shifted to the SO_3-rich side at lower temperatures
- The kinetics of the reaction at lower temperatures is very slow and below 500°C almost “frozen”

So, at lower temperatures, the SO_3 content will be maximized, but the residence time in these sections in practical applications is too short to make the conversion kinetically happen [31]. Therefore, the SO_3 content is maximized actually in a temperature field between 600°C and 800°C.

Temperature control of catalyst and substrate should be made separately. Therefore, at least two separate heating zones must be available, to guarantee a good efficiency of the test runs. For almost constant conditions in the heated areas, the mass flow should not be too high, because otherwise, the cold gases are transported through the heating area without being at the right temperature.

2.3.3 Gas Analysis

The content of SO_3 inside the gas flow changes the aggressive character of the atmosphere. The oxidation of SO_2 cannot be predicted very well, but both gases reacts at low temperature with many liquids to acid. This effect is used for the gas analysis system. Both gases should be trapped inside a media separately and afterwards, the fluids should be analysed. A standardized procedure is described by the EPA – United States Environmental Protection Agency in Method 8: Sulfuric Acid Mist [32]. The process captures the SO_2 and SO_3 in different impingers, so their content can be analyzed separately. A hydrogen peroxide solution inside a impinger is reacting with SO2 to sulfurous acid H_2SO_3. On the other hand, isopropyl and water inside a second impinger reacts with SO_3, whereas the SO_2 dissolution is inhibited inside and goes unaffected through the media. SO_3 is ionized in the presence of isopropyl to SO_4^{2-} and afterwards react with water to sulfuric acid H_2SO_4.

The content of H_2SO_3 or H_2SO_4 can be measured by a thorin-barium titration. The solutions in presence of thorin changes their colour, if barium neutralize H_2SO_3 or H_2SO_4. With knowledge of the used amount of barium, the content of SO_2 or SO_3 can be calculated with the following Equations 2.8, 2.9 and 2.10.

- Computation of the molar concentration of barium inside the barium standard solution $Ba(ClO_4)_2$ 0.01 N in mole per liter solution

$$C_{\mathrm{Ba}} = N_{\mathrm{Ba}} \cdot f_{\mathrm{eq}} \tag{2.8}$$

- SO_2 and SO_3 content inside the impinger in mole

$$\begin{aligned} n_{\mathrm{SO_2}} &= V_{\mathrm{titr(SO_2)}} \cdot C_{\mathrm{Ba}} \cdot k_{\mathrm{volume}} \\ n_{\mathrm{SO_3}} &= V_{\mathrm{titr(SO_3)}} \cdot C_{\mathrm{Ba}} \cdot k_{\mathrm{volume}} \end{aligned} \tag{2.9}$$

- Conversion rate of SO_2 to SO_3, whereas the influence of the fluid quantity inside the impingers is cancelled out

$$\frac{SO_3}{SO_2}\% = \frac{n_{\mathrm{SO_3}}}{n_{\mathrm{SO_2}}} \cdot 100\% \tag{2.10}$$

2.4 Preventive Measures for Hot Corrosion

There are many ways to improve the resistance of the system against hot corrosion. The impurities inside fuels or in the environment are the primary factor for hot corrosion. Therefore, increasing the quality of the fuel content is considered first of all. At some point, the improvement of the fuel quality is not economical enough or it is technically not feasible, so additional steps must be taken.

Particulate filters are used to remove the, for the corrosion necessary salts and other impurities out of the gas flow [4]. In practice, the amount of these particles remains too high after filtration and hot corrosion still occurs. Therefore, high-resistant bulk materials and/or protective coatings pose a lucrative alternative. Different types of material system were researched for these applications. Some progress has already been made whereas the most important improvements will be discussed throughout the next chapters [8].

2.4.1 Bulk Materials

At elevated temperatures, the materials can experience a lot of different surface changing mechanism and corrosive attacks. Resistance against hot corrosion is important, but also other properties should be analyzed to balance the decisive properties of applied materials.

A high chromium content in superalloys is desired, due to their low reaction behavior in hot corrosive media at temperatures, where LTHC occur. The formation of a uniform Cr_2O_3 oxide layer on the surface is decisive for protection against corrosion [2]. Otherwise, a high aluminum content for forming a Al_2O_3 protective layer is desirable for HTHC-resistance [4]. There are also critical elements for hot corrosion, which should be avoided in these applications. For example, higher contents of Mo inside various materials leads to severe degradation of protective films in general. Also, imperfections like NiO and CoO formations inside the oxide decrease the HC resistance and should be avoided. A pre-oxidation in controlled atmosphere leads to stable, protective chromium- and aluminum-oxides in nickel-based superalloys [24].

For high-stress conditions at elevated temperatures, for example in gas turbines, nickel based alloys like INCONEL 718 are normally used. Oxidic inhibitors like MgO, CaO and $ZnSO_4$ are reported to also lower the corrosion reaction on iron-, nickel- and cobalt-based superalloys [4].

2.4.2 Protective Coating Development

The influence of a coating system on the components surface can be enormous. The coating protects the material from outer influences and thus, resistance against hot corrosion can be improved, whereas other important material properties are unchanged. In this concept of protecting the components against hot corrosion, much research is being conducted. The variety of material systems, as well as the coating techniques, are enormous. For example, electron beam physical vapor deposition and high velocity oxygen fuel spraying (HVOF) are the most important techniques for these applications.

One of the most promising approach is a MCrAlY-based coating, where M can be nickel, cobalt or a combination of both. Especially, the resistance against hot-corrosion Type II is very well known, due to the high content of chromium. This coating system is frequently used for bonding layers of thermal barrier coatings, where the TBCs improve the oxidation resistance and the metallic bond layers are decisive for resistance against other corrosive processes [11, 33]. Also, platinum aluminide coating with HVOF improve the hot-corrosion resistance on titan alloys. The platinum serves as interlayer with aluminide coating on top [8, 34].

Investigations of other coating systems are on track to increase the lifetime of attacked components. A procedure with high potential for protective layers is the physical vapor deposition technique [11]. Coating systems like $Ti_{0.51}Al_{0.49}N$ or $Cr_{0.9}Si_{0.1}$ are used for other high temperature applications and therefore, the inertness of such coatings against hot corrosion should be analyzed.

Chapter 3

Design and Construction of CORA

At initial stage, the construction of a Corrosive Oven for Research and technical Applications (CORA) should be complied with many conditions. The most important ones should be mentioned:

- The furnace must provide a temperature range inside the reaction chamber, where hot corrosion occurs (600°C to 950°C).
- A SO_x rich atmosphere with a constant gas flow must be established without removing the salt deposits from the material surfaces that are under investigation.
- The tubing system have to be resistant against aggressive gases such as SO_2 and SO_3.
- The gas flow components have to be constructed inside a fume hood, for safety reasons. If leakage problems occur throughout the gas supply system, the hazardous gases must be kept away from working personnel.
- The control panels are installed in safe areas of the construction, so outside of the fume hood.

The development of the construction plan is described in the next chapters. Before the individual components can be described, an overview of the most important system sections is presented in Figure 3.1. To fulfill the condition of the working area inside a fume hood, a compact construction is necessary. The structure is designed in three levels:

- A bottom section, where the gas analysis system and cleaning process takes place
- A middle section, which is mounted under the worktable, the gas mixing system is positioned

- A top section, stationed on top of the worktable, where the furnace and reaction chamber are placed

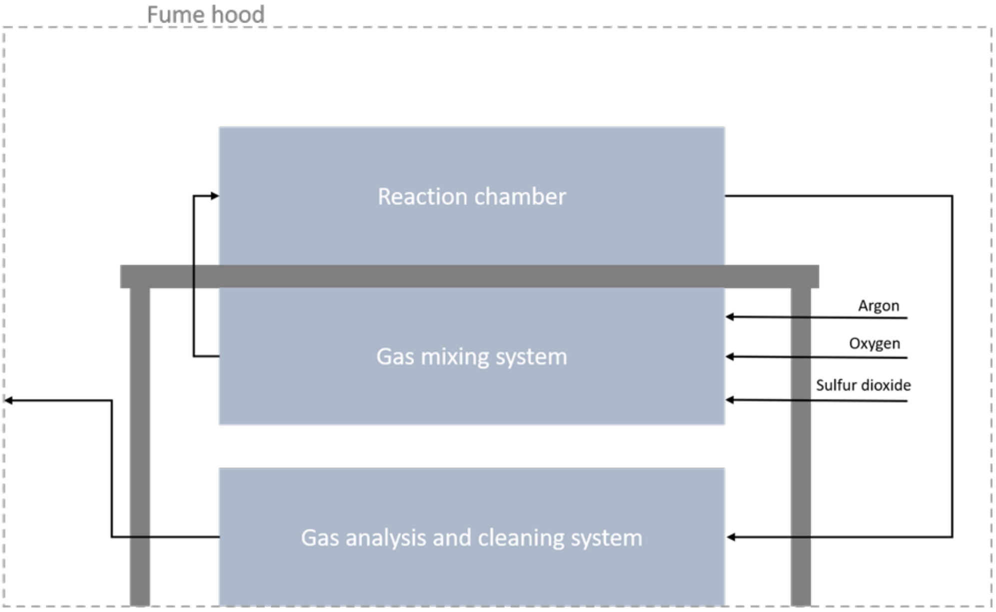

Fig. 3.1: Schematic representation of CORA.

3.1 Gas Mixing System

This part of the testing system is necessary to mix argon, oxygen and sulfur dioxide with various proportions. Each of the gas flow is drawn from a separate gas cylinder and is adjusted individually. For safety reasons, the sulfur dioxide gas cylinder is placed inside the fume hood. The other two gas cylinders were placed outside the fume in a gas cabinet. Both gases are directed inside the fume hood with a separate tube system.

Due to the aggressive nature of SO_2, the choice of the material used for the tube system should be caried out carefully. As pipe material, PFA (perfluoro-alkoxy-alkanes) was opted for, because of its chemical inertness against most corrosive gases. The downside of this material is the limiting temperature of about 260°C and the low maximum working pressure of around 3.3 MPa at 20°C. The connection parts between gas mixing system and the furnace system are the most critical construction units against temperature. Therefore, these components are not used in direct vicinity of the furnace and the temperature there is controlled frequently. For not exceeding the maximum working pressure, reducers on the gas cylinders are necessary. The individual components of the gas mixing system will be discussed below. A detailed sketch of the gas mixing system is illustrated in Figure 3.2, Figure 3.3 and Figure 3.4, where the blue lines indicate the pipelines.

The first components inside the pipe system, which should be mentioned, are the manual valves. Every gas type has their own manual valve to open and close the gas supply. An additional valve is mounted in the connection pipe between the Ar and SO_2 gas installment. This gives the opportunity of purging the SO_2 part of the system with Ar and so, the components are not always in contact with the aggressive gas.

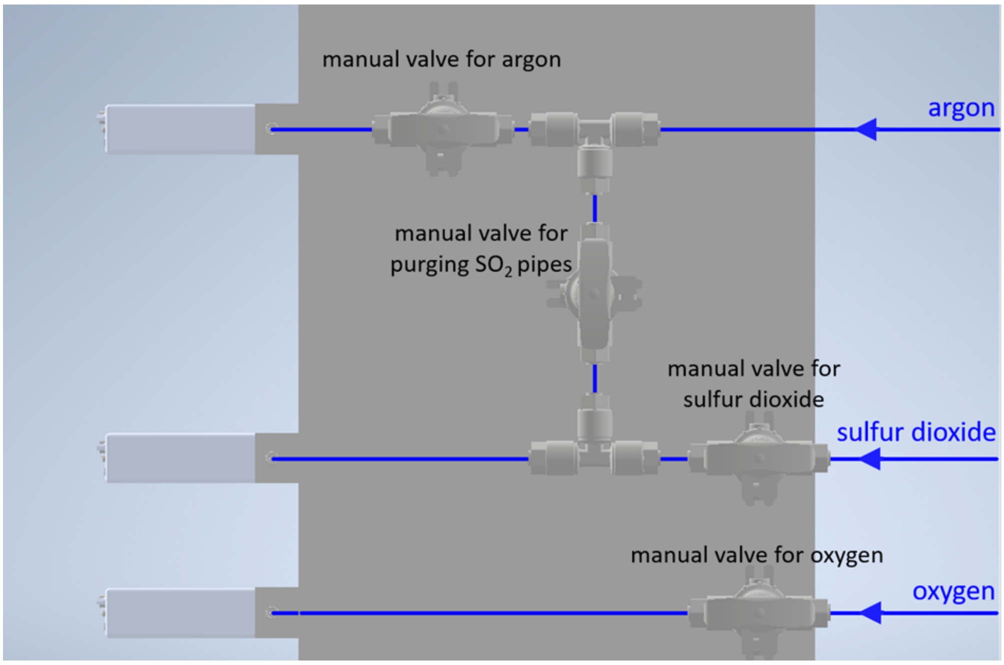

Fig. 3.2: Gas mixing system in front view.

The flow rate of the gases should be designed in such manner, that the total gas volume inside the chamber is renewed frequently, but the gas flow remains subtle enough, not to flush the salt deposits from the sample surfaces. Therefore, the velocity of the gas flow was chosen such, that a complete replenishment of the gas volume (purging of the reaction chamber) may proceed within one minute. With a total volume of the reactor being 2500cm3, the necessary total gas flow must provide an input of 2500 standard-cubic-centimeters-per-minute (sccm). For every gas supply, a separate mass flow controller (MFC) for Ar, O_2 and SO_2 is integrated, sketched in Figure 3.3.

The chamber is purged only with argon and so, the dimensioning of the Ar mass flow is set to 5000 sccm (complying the 2500 sccm for replenish the chamber within one minute). Argon is used as a carrier gas in order to distribute the other components of the gas system uniformly. The ratio of O_2 and SO_2 is clearly at the oxygen side in technical applications. Therefore, a 50:1 ratio of O_2:SO_2 at the maximum value of each MFC is configurated. The SO_2 content in gas turbines is in the range of parts per million (ppm), but the corrosion process needs a long time to proceed. The maximum test duration is about 1 to 3 hours, so the SO_2 content has to be adjusted for obtaining noticeable results. The chosen maximum mass flow for SO_2

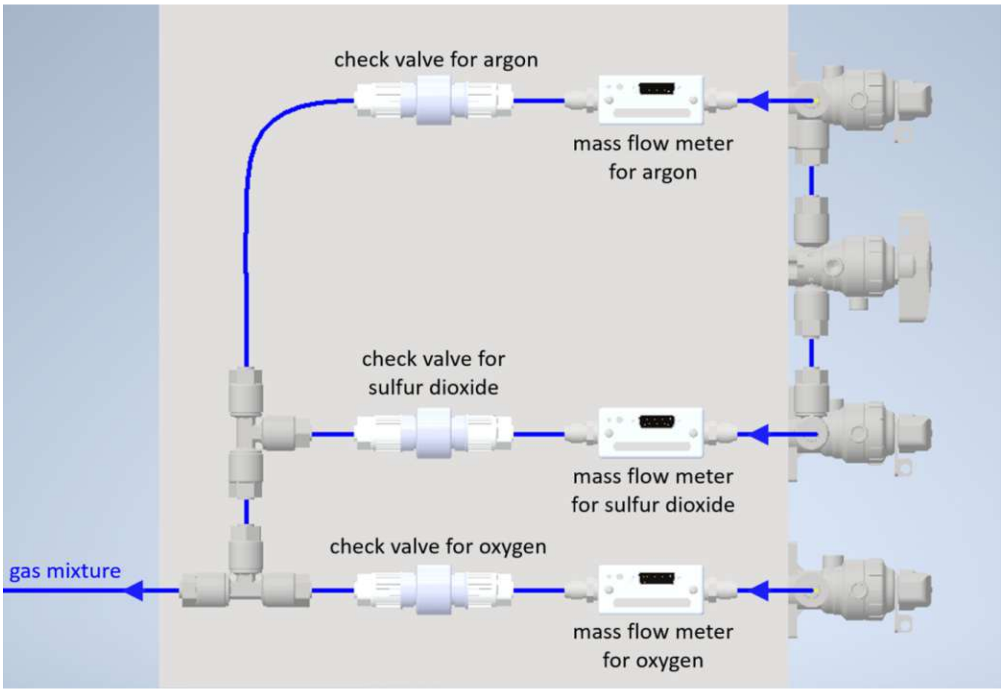

Fig. 3.3: Side view of the gas mixing system.

is 10 sccm and consequently, for the testing process a SO_2 content of 1815 ppm for maximum mass flow of each gas, according to Equation 3.1.

$$\phi_{\mathrm{SO_2}} = \frac{\dot{V}_{\mathrm{SO_2(max)}}}{\dot{V}_{\mathrm{Ar(max)}} + \dot{V}_{\mathrm{O_2(max)}} + \dot{V}_{\mathrm{SO_2(max)}}} \cdot 10^6\ ppm = 1815\ ppm \tag{3.1}$$

The duration of purging the SO_2 gas tubing system with Ar takes quite a long time, due to the very low maximum mass flow of 10 sccm (applied with Ar). Therefore, the purging process of the SO_2 tubing system with Ar should not be made after every test run.

The oxygen maximum level is set 50 times higher with 500 sccm, planned with the theoretical background of chapter 2.3.1. With these settings, the maximum velocity inside the gas pipe systems and the quartz reactor can be calculated, according to Equation 3.2.

$$\begin{gathered}
\dot{V}_{\mathrm{max}} = \dot{V}_{\mathrm{Ar(max)}} + \dot{V}_{\mathrm{O_2(max)}} + \dot{V}_{\mathrm{SO_2(max)}} = 5510\ sccm \\
v_{\mathrm{pipe}} = \frac{4 \cdot \dot{V}_{\mathrm{max}}}{d_i^2 \cdot \pi} = \frac{4 \cdot 5510\ sccm}{6.35\ mm^2 \cdot \pi} = 2.9\ \frac{m}{s} \\
v_{\mathrm{reactorpipe}} = \frac{4 \cdot \dot{V}_{\mathrm{max}}}{d_i^2 \cdot \pi} = \frac{4 \cdot 5510\ sccm}{55\ mm^2 \cdot \pi} = 0.039\ \frac{m}{s}
\end{gathered} \tag{3.2}$$

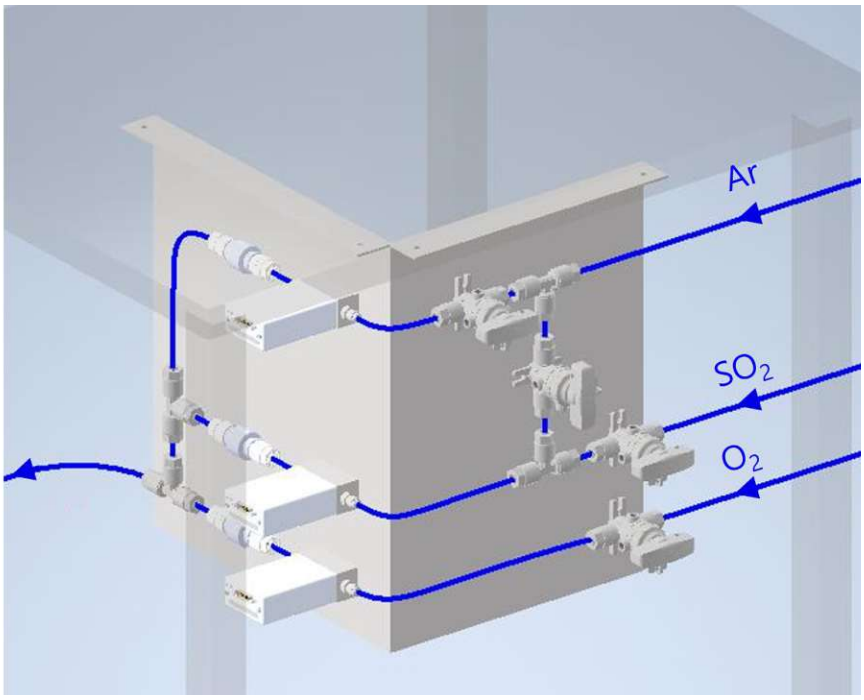

Fig. 3.4: Construction of the gas mixing system, mounted under the worktable.

For the non-corrosive gas flow meters, the standard sealing, which consists of VITON, are used. On the other side, a more protective sealing material EPDM is used for SO_2 pipe system. A mass flow meter, which can be controlled from outside of the fume hood, is necessary due to safety reasons. Therefore, a GE50A from MKS instruments is used as mass flow controller (MFC), which fulfill the conditions. A picture of the MKS GE50A is given in Figure 3.5.

Fig. 3.5: MFC massflow controller GE50A used in the gas flow system.[35]

As the control panel, a JEVATEC Jevaflow FCU-4 is used, which can be connected with all MKS mass flow meters. Another benefit of the JEVATEC controller is the easy handling. The control panel is pictured at Figure 3.6.

Fig. 3.6: The control panel JEVATEC FCU-4, which is responsible for the gas flow regulation.[36]

The last important component to be discussed, is the check valve after the mass flow controller, seen in Figure 3.3. The flow inside the mass flow controller must be in one direction, which is indicated on the MFCs (compared to Figure 3.5). Also, the argon and oxygen mass flow meter should not come in contact with the reactive gas SO_2, because of their non resistant sealing elements. The check valves guarantee the flow in the right direction.

3.2 Reaction Chamber

There are many different possibilities to develop the chamber atmosphere. The first question to deal with is the gas flow inside the furnace. Without having a gas flow inside the reaction chamber, the gaseous media will be consumed quickly and the severity of the corrosive atmosphere will decrease with time, so the procedures can´t be reproduced very well. For constant conditions inside the chamber, it should be floated constantly, hence a horizontal tube furnace was selected.

A quartz glass reactor was a reliable choice for these requirements. A downside of quartz glass is its brittle properties against higher pressure and inside vacuum. High pressure gases, coming from the gas cylinders, are reduced by the MFCs and so, the pressure inside the quartz glass reactor is approximately at ambient pressure level (1 atm). Therefore, a vacuum pump, which clean-up the atmosphere inside the reactor is not feasible and an alternative cleaning concept has to be developed. The quartz glass reactor is cleaned thoroughly. After mounting it in the furnace, the reactor should be purged with Ar and subsequently heated, to neutralize the atmosphere in the inner parts. Differences between the optimum temperatures for the catalyst and hot corrosion temperatures are provided with a gradient furnace having different temperature zones – as the best solution for this application. A three-zone EZS-3G Carbolite furnace was selected (see Figure 3.7).

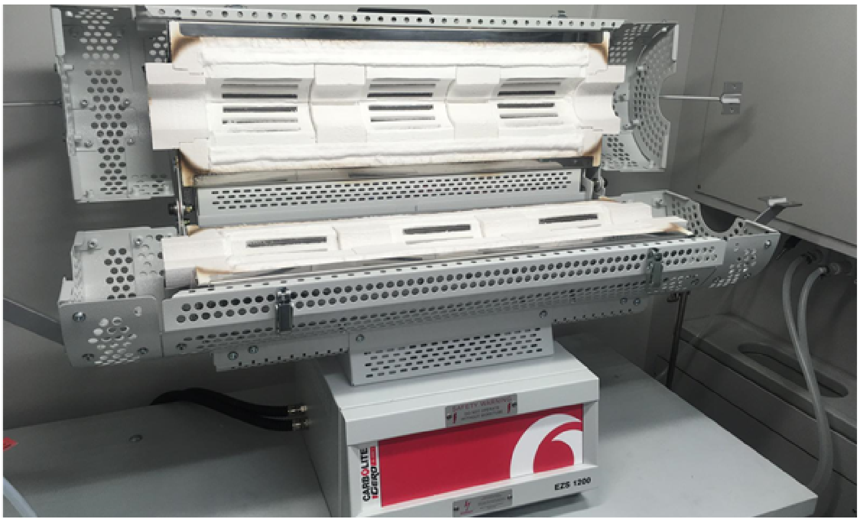

Fig. 3.7: Carbolite EZS-3G floating furnace inside the fume hood.

For this furnace system, a quartz glass reactor with 55-millimeter inner diameter and a length of 1.1 meter was chosen. An example for the temperature profile inside the furnace is illustrated in Figure 3.8. Each zone has their own task inside the corrosion system, which will be described accurately below.

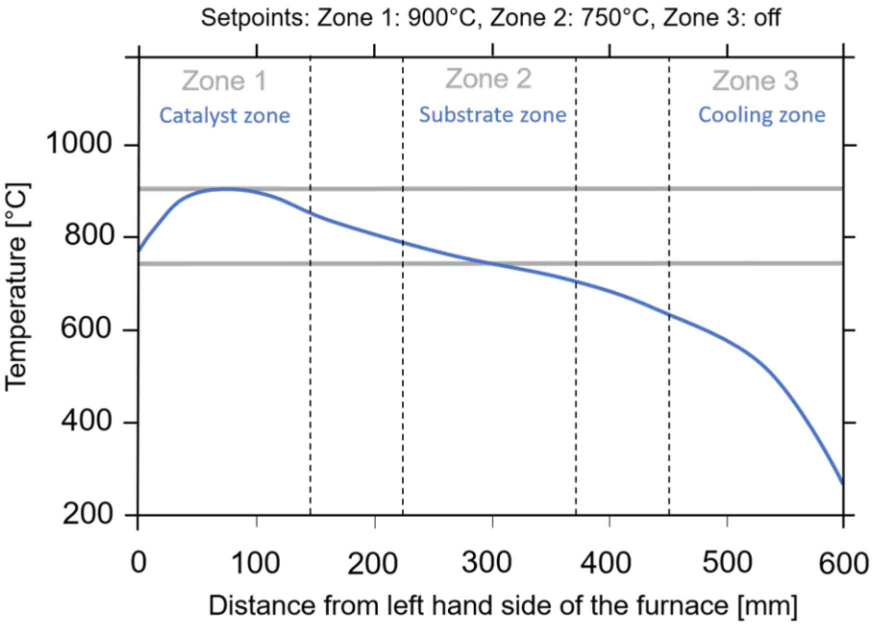

Fig. 3.8: Example of temperature curves inside the three-zone furnace, adapted from [37].

In gas engines systems, the SO_3 transformation is accelerated with flying particles inside the gas flow. This catalytic effect is very important for the corrosion process, due to the high reactivity of SO_3 on most metals. Flying particles, which are often ash products from the combustion chamber, would cause many problems inside the chamber. So, another possibility of catalytic effect must be considered inside the quartz reactor. A iron-oxide wool catalyst is optimal for our application, due to the large surface and material similarity with parts of fly ash particles (based on chapter 2.3.1). The catalyst is mounted at heating Zone 1, whereas the temperature is adjusted between 600°C and 700°C for an ideal catalytic effect.

Zone 2 is the substrate area, where the corrosion process occurs. The dimensions of austenite substrates are 20x7x1.5 mm and for IN718 substrates 20x10x5 mm. For every run, two sample holders are needed:

- Sample holder with substrates in horizontal positions, where salt is deposited on the surface before testing. The construction for 4 substrates is sketched in Figure 3.9.
- Sample holder with substrates in vertical position without salt contamination, see Figure 3.10.

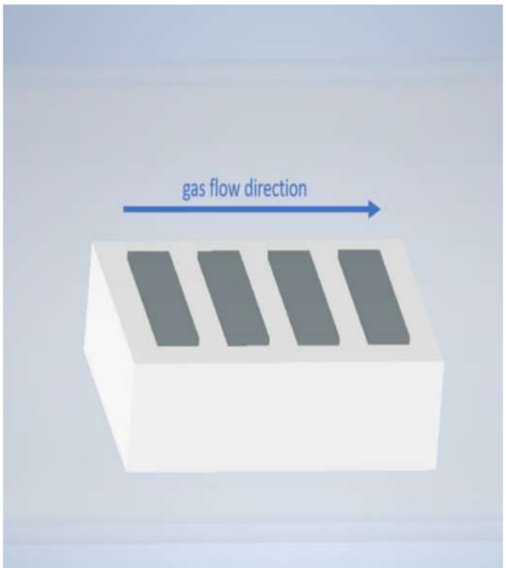

Fig. 3.9: Substrate holder at horizontal position, where the salt mixture can be placed on the substrate surface.

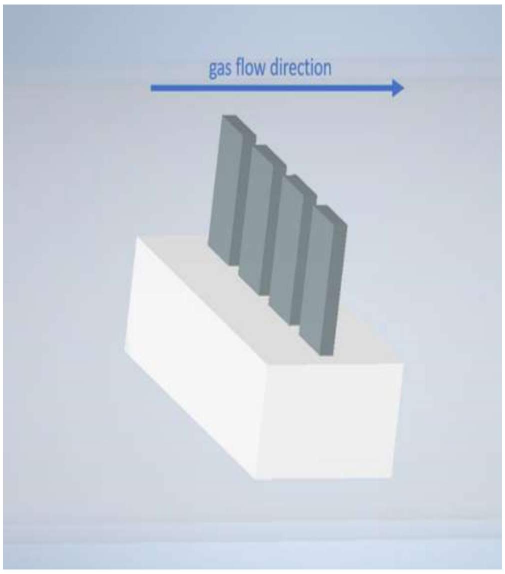

Fig. 3.10: Substrate holder at vertical position with mounted substrates.

The substrate holder with the vertical samples is positioned in front of the horizontal substrate holder, so the salt mixture cannot influence the standing samples. The vertical substrates serve as references for the hot-corroded probes.

Inside the last zone, also samples can be mounted at lower temperatures. With higher temperatures at Zone 3, the gas temperature at the quartz reactor exit is elevated and heat-up the PFA pipeline between furnace and gas analysis system. The allowed temperature for

PFA tubes is limited and therefore the pipes can be damaged. With the last zone heated-up, the temperature of the outlet gas must be monitored for the whole test run. In most cases, Zone 3 is utilized as cooling down length for lower temperatures after exiting the furnace.

3.3 Gas Analysis System and Cleaning Process

The gas analysis is orientated on the EPA method 8, as described in chapter 2.3.3. The procedure is modified for the testing applications in this study to improve the accuracy of the gas analysis system. In other testing systems, H_2O is also carried inside the gas flow and therefore, in EPA method 8 the condensation temperature of H_2SO_4 should be considered. Otherwise the sulfuric acid goes in liquid state and remains inside the pipe system. With the absence of H2O inside the construction of CORA, the temperature inside the pipe system can be cooled to room temperature, Also, a recommended vacuum pump is not necessary because of the high-pressure difference of the gas cylinder reducers and the pressure after the gas analysis system (ambient pressure).

The gas flow goes through four collecting impinger bottles, where the SO3 is caught by a mixture of 80% isopropyl alcohol + 20% deionized water in impinger 1 (Figure 3.11). The content of SO_2 is captured inside the impingers 3 and 4 filled with 3% H_2O_2, which is diluted with deionized water. The two different measurements should not be influenced by each other and therefore, the empty impinger 2 is placed between both analytical sequences to avoid any contamination. The impingers are embedded inside a cooling box with ice water in order to effectively capture the entire SO_3 and SO_2. For cleaning the last residues of the corrosive contents inside the gas flow, a gas cleaning impinger filled with NaOH is installed. Afterwards, the gas flow goes inside a disposal for exhaust gases.

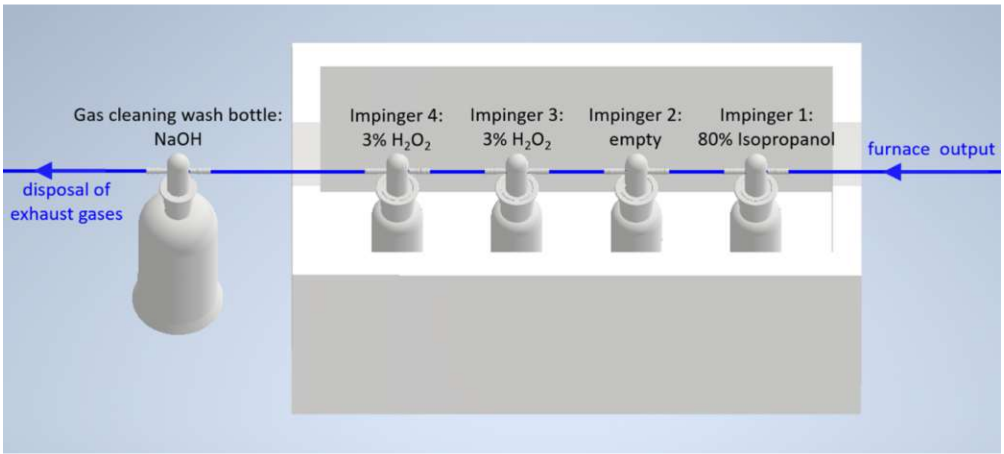

Fig. 3.11: Construction of the gas analysis and cleaning system, where blue lines intend the pipeline.

Chapter 4

Experimental

4.1 Deposition of Thin Film Layers on Austenitic Steel

For testing the reliability of CORA, besides bulk materials like austenitic steel and INCONEL, different PVD coating systems were considered and tested. For the tests in this thesis, a $Ti_{0.51}Al_{0.49}N$ coating with ceramic character and a metallic $Cr_{0.9}Si_{0.1}$ coating were deposited on austenitic substrates. The $Cr_{0.9}Si_{0.1}$ layer was produced by high power impulse magnetron sputtering (HiPIMS). The deposition of $Ti_{0.51}Al_{0.49}N$ was performed via a cathodic arc-evaporation technique. Because of their different characteristic, the coatings are very diverse, so the information value of the testing rig reliability is improved. The deposition parameters for both coatings are summarized in Table 4.1.

Table 4.1: Deposition parameters of the coating processes.

chemical composition [at.%]	substrate temperature [°C]	Bias [V]	atmosphere [µbar]	PVD technique	coating thickness [µm]
$Ti_{0.51}Al_{0.49}N$	450	-40	32 (N_2)	cathodic arc-evaporation	4.2
$Cr_{0.9}Si_{0.1}$	300	-100	4 (Ar)	HiPIMS	4.1

The $Ti_{0.51}Al_{0.49}N$ coatings on austenitic steel were developed utilizing an Oerlikon Balzers INNOVA coating system. Before the deposition process takes place, a careful polishing and cleaning process of the samples were executed. Afterwards, the samples were mounted inside the substrate holder of the respective deposition system and the chamber was evacuated, to reduce the collision probability between ions and atoms during the coating process. For removing the last residual debris on the substrate surface, a standardized CBE etching process was executed. For an optimal deposition procedure, the depositing parameters were optimized frequently during the process, according to Table 4.1. The process was controlled by the cathodic current, which is set to 200A. After the deposition process, the system was cooled down and the samples were dismounted and cleaned. Lastly, the deposition data were logged for comprehensibility of the deposition process.

In contrast, the $Cr_{0.9}Si_{0.1}$ thin films were synthesized on a NOREIA HiPIMS deposition system. The preparation of the samples was similar to the $Ti_{0.51}Al_{0.49}N$ preparation procedure. The etching process was accomplished at 60 μbar in Ar flow (60 sccm), with VS = -1000V bias potential on the substrate. The HiPIMS deposition process is utilized at 75 Hz pulse frequency with a pulse duration of 75 μs and an average target power of 1.5 kW, for the coating establishment. Afterwards, the chamber was cooled down and the samples were gathered and cleaned. As mentioned at the $Ti_{0.51}Al_{0.49}N$ coating, the whole process was monitored and the data were logged.

4.2 Hot Corrosion Testing

4.2.1 Temperature Calibration

An accurate substrate temperature is very important for the comparability with other studies. The furnace temperature can be set at each heating stage (furnace Zone 1, Zone 2 and Zone 3). There will be a temperature offset between the furnace thermocouples – which are set by the controller - and the temperature inside the reactor, given with Equation 4.1.

$$\Delta T_{\text{substrate}} = T_{\text{furnace}} - T_{\text{substrate}} \tag{4.1}$$

For measuring this temperature offset, thermocouples are mounted in different position inside the chamber as well as on the outer side of the tube. The furnace was heated up with different temperatures and flowrates, pictured in Figure 4.1. The inside temperature can only be analyzed in absence of SO_2 because otherwise the instruments would corrode. Also, the possibility of leaking problems in the instrumental lead-through make a measurement under harsh conditions difficult. At furnace Zone 1, the temperature of the catalyst is measured with the thermocouple T1. Thermocouple T2 is integrated for measurements of the substrate temperature (Zone 2). Due to the temperature limit of PFA tubes at 260°C, the thermocouples T3 and T4 are installed for safety reasons. Hence, the process will be stopped when the PFA tubes get heated-up to 200°C.

The temperature range for hot corrosion (600°C to 950°C) is tested with varying mass flows (500 sccm to 5000 sccm). For the experiments in this thesis, the calibration of 650°C and

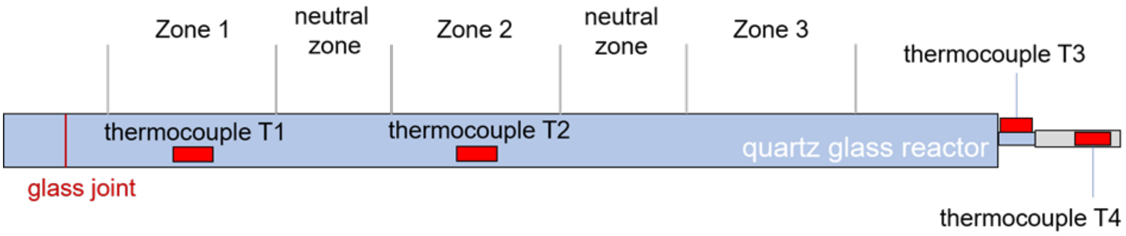

Fig. 4.1: Positioning of the thermoelements for temperature calibration.

850°C at Zone 2 (temperatures according to the furnace controller) are of primary interest, as these temperatures ultimately dictate the type of corrosion that occurs within the reactor (LTHC = 650°C, HTHC = 850°C). The catalytic section (Zone 1) is heated-up to 600°C and 700°C. The results of the calibration are given in the following charts (Figure 4.2 and Figure 4.3).

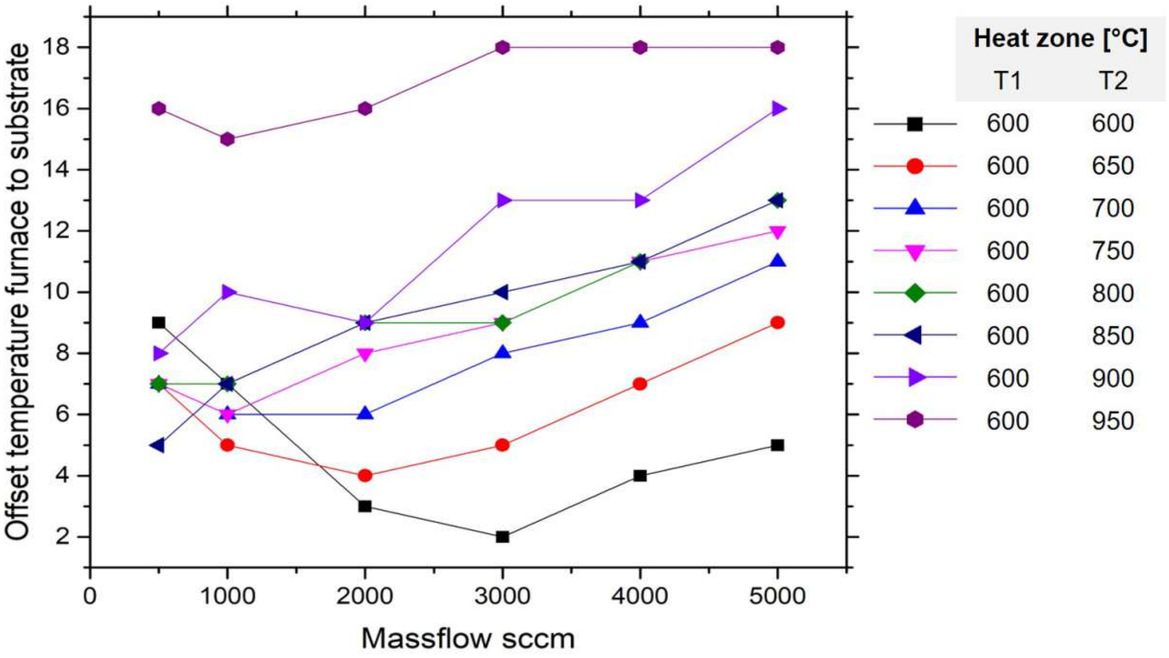

Fig. 4.2: Offset temperature between furnace controller temperature and thermocouple inside the tube at 600°C in the first zone measured with thermocouple T1 and varying the temperature for second zone measured by thermocouple T2.

The temperature offset rises with higher temperature difference between Zone 1 and Zone 2. So, for equal temperature in both heating zones, the temperature offset is negligible. For higher temperatures in Zone 2, the offset increases, may be due to a lower gas flow temperature inside Zone 1, which then enters Zone 2. The residence time inside the zone is not enough, to heat the gas flow up to the set temperature needed.

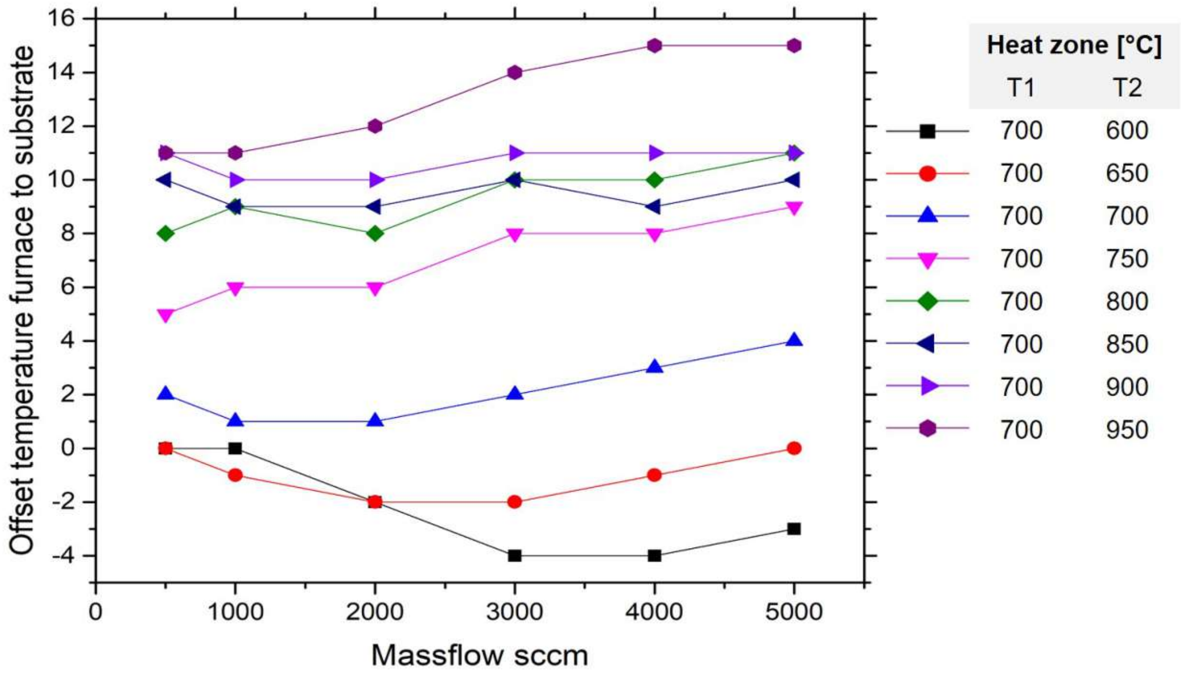

Fig. 4.3: Offset temperature between furnace controller temperature and thermocouple inside the tube at 700°C in the first zone measured with thermocouple T1 and varying the temperature for second zone measured by thermocouple T2.

Also, with a higher mass flow, the temperature influence of Zone 1 on the substrate (Zone 2) becomes noticeable. Ultimately, the aim of these temperature calibration experiments is to establish an understanding about the relationship between the heating zones and how different mass flows influence the thermal gradients with the reaction tube. For test runs with temperatures and/or mass flows, which have not been calibrated, data from earlier measurements can then be interpolated in order to make a reasonable estimation about the actual substrate temperature.

By measuring the temperature at the quartz glass reactor outlet, where the connection with the tube system is applied, the limiting temperature of 200°C was never recorded using the thermocouples T3 and T4. The highest temperatures observed at T3 and T4 was 141.2°C/167.9°C, respectively at the configuration 700°C (Zone 1) and 950°C (Zone 2) with an Ar flow of 5000 sccm.

4.2.2 Gas Analysis Titration

The oxidation of SO_2 to SO_3 is one of the key reactions for hot corrosion. Hence, having knowledge about the conversion ratio of SO_3/SO_2 within the reaction chamber is an important piece of information when trying to assess the corrosion behavior of protective coatings. For measuring the SO_2 and SO_3 fractions of the atmosphere within the reaction chamber, the standardized method 8 of EPA was utilized (chapter 2.3.3).The gas analysis was tested for different temperatures and flowrate settings, respectively.

Before turning on the furnace, certain steps in preparing the gas analysis had to be followed. Propanol, diluted with deionized water with a volumetric ratio of 80:20 (propanol:water), was filled into the first impinger to catch the SO_3. The second impinger was left empty, due to the possibility of splatter contamination between impingers. The third and fourth impinger were filled with 3 vol.% H_2O_2 in deionized water. All three impingers were filled with 100 ml of their respective solution.

After completing a test run, the analysis of the gas composition was conducted using a barium-thorin titration. The first impinger was diluted with 80 vol.% propanol to 250 ml. Afterwards, a 10 ml aliquot of the new solution was taken and a drop of thorin was added. At this point, if any SO_3 was present within the propanol aliquot, the color should show a light yellow. To quantify the amount of SO_3 inside, a standard barium solution (0.01N) was titrated drop by drop until color transition from yellow to pink was observed. With the molar equivalent of barium perchlorate, the quantity of SO_3 can be calculated.

For the detection of SO_2, the contents of the third and fourth impingers were combined and diluted to 250 ml. After dilution, an aliquot of 10 ml taken and titrated with the barium standard solution (0.01N) until a color transition of the thorin indicator was observed. Similar to the SO_3 titration process, the color change indicates the endpoint and the SO_2 content can be determined.

4.2.3 Testing Process of Different Substrates

To demonstrate that CORA fulfills all requirement, a variety of samples was tested. Two different bulk materials were tested for their corrosion behavior within the testing rig: austenitic steel as well as IN718. Furthermore, $Ti_{0.51}Al_{0.49}N$ and $Cr_{0.9}Si_{0.1}$ coatings deposited on austenitic steel substrates, were examined inside CORA for more validity. In addition, so-called reference measurements without SO_2 inside the testing atmosphere were performed too. A salt mixture of NaCl-Na_2SO_4 with a 70:30 ratio, respectively, was used for every test run. The total mass flow was set to 2500 sccm, so a gas velocity inside the quartz reactor of approximately 1 meter per minute was achieved. The SO_2 content inside the gas flow was limited to 1000 ppm by the respective MFC, which results in a flow rate of 2.5 sccm. The duration of the experiments, after purging and heat-up for verifiable conditions, was always set to 60 min. The temperature in heating Zone 1, where the catalyst was placed, was set to 600°C in every experiment.

An overview of the tested substrates for HTHC conditions is given in Table 4.2. These experiments were performed at 850°C at the substrate Zone 2.

Table 4.2: Substrate and testing parameters for HTHC experiments in CORA

	Bulk Material	Coating System	Temperature at Zone2 [°C]	Ar [sccm]	Atmosphere O_2 [sccm]	SO_2 [sccm]
HTHC Run1	Austenite	uncoated	850	2125	375	0
	IN718	uncoated	850	2125	375	0
HTHC Run2	Austenite	uncoated	850	2122.5	375	2.5
	IN718	uncoated	850	2122.5	375	2.5
HTHC Run3	Austenite	$Ti_{0.51}Al_{0.49}N$	850	2122.5	375	2.5
	Austenite	$Cr_{0.9}Si_{0.1}$	850	2122.5	375	2.5

Also, LTHC experiments were conducted at 650 °C, which detailed parameters are listed in Table 4.3.

Table 4.3: Substrate and testing parameters for LTHC experiments in CORA

	Bulk Material	Coating System	Temperature at Zone2 [°C]	Ar [sccm]	Atmosphere O_2 [sccm]	SO_2 [sccm]
HTHC Run1	Austenite	uncoated	650	2125	375	0
	IN718	uncoated	650	2125	375	0
HTHC Run2	Austenite	uncoated	650	2122.5	375	2.5
	IN718	uncoated	650	2122.5	375	2.5
HTHC Run3	Austenite	$Ti_{0.51}Al_{0.49}N$	650	2122.5	375	2.5
	Austenite	$Cr_{0.9}Si_{0.1}$	650	2122.5	375	2.5

The testing procedure was kept identical for each corrosion experiment. The samples and the pipe system were cleaned and the samples were mounted on a clean aluminum oxide substrate holder. After mounting the samples, a mixture of NaCl-Na_2SO_4 salt was dissolved in deionized water and dripped on the horizontally positioned substrate surfaces. After each corrosion experiment, the substrate holders were exchanged for new ones, to avoid any cross contamination from previous runs.

The sample holders were placed in Zone 2 inside the quartz tube. The iron-oxide wool catalyst was placed in Zone 1. The gas analysis and cleaning system were prepared accordingly. The gas flow system and the quartz reactor were connected again.

At this point, all necessary preparation steps were finished, and the actual experiment was started. The system was purged with 2000 sccm Ar gas. After 10 min, the whole system should be cleaned up and the furnace was turned on. To make sure, the reaction chamber is evenly heated-up, the furnace should run for at least one hour, before injecting the desired corrosive atmosphere. The corrosion process was started with adjusting the gas flow for argon, oxygen and sulfur dioxide, whereas the sulfur dioxide valve should be the last one to be opened. After the test run, the system has to be cooled down to room temperature. Afterwards, the quartz glass reactor was dismounted. The gas cleaning system was disconnected from the pipe system and the cleaning fluids were disposed. The entire system together with the corroded samples were cleaned. Lastly, the samples were recorded visually and the testing process was put to protocol.

4.3 Analytical Techniques

To verify the results of the test runs, different analytical techniques were used. The first very simple but meaningful method is a visual inspection of the samples. Corrosive products, which do not adhere on the surface, were collected and stored separately. Samples were cleaned inside an ultrasonic bath with ethanol and deionized water in order to remove any excess NaCl-Na_2SO_4 salt-slag deposits. After the first preliminary analysis, the samples were investigated by X-ray diffraction (XRD), scanning electron microscopy (SEM) and energy dispersive X-ray spectroscopy (EDS). Each method will further be discussed throughout the next sections.

4.3.1 X-ray Diffraction

A very important characterization step of corroded samples is X-ray diffraction analysis (XRD), where the crystal structure on surface near areas can be determined. The crystal structure provides information of the formed corrosion products in surface regions of the material. In this thesis, the detection method is using a Bragg Brentano high definition

(BBHD) focus geometry to obtain the crystal structure in surface near areas of the samples. The samples are not influenced by this analytic method and so, XRD should be made before the samples are embedded for further destructive analysis.

A monochromatic X-ray beam is directed toward the specimen in different angles. A cathode ray tube generates X-rays and with applying a potential difference on the target, the X-rays are accelerated toward the specimen. Inside the material, the X-rays are diffracted by the crystal structure of the material. A detector collects the diffracted X-rays. At determined angles, the reflected X-rays produce constructive interference, which are indicated for the interplanar spacing of atoms. Constructive interference occurs, if Bragg´s law is fulfilled, given in Equation 4.2.

$$n \cdot \lambda_{\text{X-ray}} = 2 \cdot d \cdot sin(\theta) \tag{4.2}$$

This law gives the relation between wavelength $\lambda_{\text{X-ray}}$ and the lattice spacing d in the crystal structure under consideration of the beam angle θ and n as positive integer. In practice, the specimen is scanned by an X-ray beam angle range with a determined wavelength. The reflected X-rays are simultaneously collected by a detector, whereas the intensity of constructive interference of X-rays are measured. Afterwards, the interplanar spacing is calculated and so, crystal structures and phases can be interpreted. The interpretation is typically made by a comparison with standard reference measures [38].

4.3.2 Scanning Electron Microscopy and Energy Dispersive X-Ray Spectroscopy

In order to visualizing the cross-section of the corroded samples, a scanning electron microscope (SEM) was utilized. Before analyzing inside the SEM, sample preparations had to be made. The samples where embedded in an electrically conductive polymer. For analyzing the middle section of the substrate, a grinding process was needed, to reach this section. Afterwards, the surface was polished to smoothen the surface in order to avoid any scattering of the electron beam inside the SEM. After preparation, the samples were analyzed in the SEM. This analysis technique was used for many different applications, because of the high informative value in topography and composition in surface near regions of the material. The principle of this investigation is based on an electron bombardment of the material at hand, whereas the electrons are generated by a so-called electron gun. The specimen chamber is at vacuum to reduce the interactions between atoms of the atmosphere and the electrons. Applying a potential difference between the electron gun (cathode) and the anode leads to an acceleration of electrons toward the substrate. The electrons are directed through electromagnetic lenses, while a deflections system focuses the beam onto a small area of the material. This electron beam then collides with the specimen electrons, resulting in different radiations of the material. These signals can be analyzed by detectors in many ways. The most common signal detections are based on the radiations of secondary electrons (SE) and backscattered electrons (BSE) [39, 40].

- Secondary electrons (SE) are weakly-bonded electrons, which can be ejected out of the material in surface near areas by inelastic electron collisions inside the material. These electrons have a low kinetic energy of 3-50 electron volts.
- Backscattered electrons (BSE) result from an elastic collision of electrons. The primary electrons - coming from the electron gun – are redirected inside the material to the surface and are detected again. The intensity of the BSE is depending on the material composition. The kinetic energy is much higher compared to SE.

An energy dispersive X-ray spectroscopy (EDS) system is also included inside the SEM and therefore, the microscopy and EDS analysis were made in the same procedure. EDS is based on measuring characteristic X-rays, generated by electrons, which changes position from an outer shell of an atom to a vacancy at the inner shells. The electron vacancy is a result of a bombardment with an electron beam. The quantity of emitted energy at the transition event is characteristic for an element type, which can shed light on the material composition at the focused point [40].

Chapter 5

Results & Discussion

5.1 General Investigations

First, the samples were visually inspected without any technical devices. The typical characteristics for HTHC and LTHC were observed as corrosion products formed on top of the substrate surfaces. The material surfaces were covered with a porous, fragile layer. Beneath this layer, a roughened material surface appeared, which had little in common with the original state. Top view images of uncoated IN718 and austenitic steel after various experimental executions are illustrated in Figure 5.1 e-t. The original, uncorroded state of the bare samples are shown in the first row, see Figure 5.1 a-e. Oxidized samples, without SO_x content inside the gas flow are arranged at second row (Figure 5.1 e-h), in the middle section substrate surfaces in O_2+SO_2 atmosphere at 650°C are displayed (Figure 5.1 i-l), and at the last two rows, samples without and with SO_x in 850°C experiments are shown (Figure 5.1 m-t). The images were collected using a Keyence VHX 6000 digital microscope. Samples with Na_2SO_4 were tested in horizontal substrate holders, so that the salt deposits can better adhere to the sample surface. Contrary, test substrates without Na_2SO_4 were mounted in a vertical version. It is important to mention that one end of the standing sample (left side of pictures) was plugged inside the holder and therefore, these areas look different compared to the material surface that stood in direct contact with the corrosive atmosphere.

In absence of Na_2SO_4/NaCl salt, the surfaces of IN718 changed in color at higher temperature, but an overly accelerated development of corrosion products was not observed. For IN718 samples, which experienced corrosion with the Na_2SO_4/NaCl salt mixture on their surface, porous layers formed at the surface, e.g. see Figure 5.1 j with Na_2SO_4. The influence of the SO_x content was also investigated, which can clearly be seen throughout Figure 5.1 and Figure 5.2, where the attack becomes more aggressive and pronounced in presence of SO_x. The occurrence of the corrosive attack was detected very well for IN718. Under LTHC conditions, a clear manifestation of a pitting mechanism was observed (Figure 5.1 j). For the

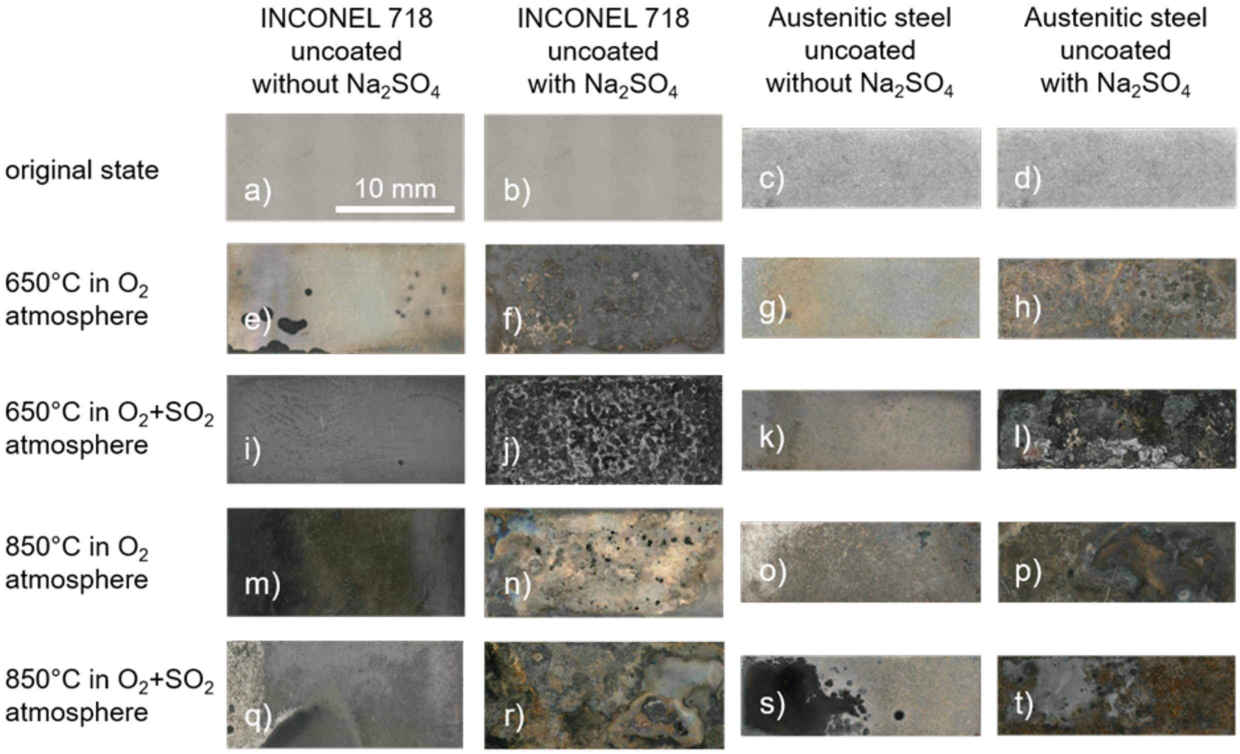

Fig. 5.1: Top view images of uncoated samples (IN718 as well as austenitic steel) after different testing conditions.

HTHC experiments, a more uniform corrosive attack can be seen (Figure 5.1 r).

In the case of austenitic steel, experiments in absence of SO_x and salt deposits exhibited slightly oxidized surface states, indicated by slight tempering colors, seen in Figure 5.1 g and o, respectively. For experiments with salt deposits however, a very aggressive corrosion attack, independent on the temperature, was developed (Figure 5.1 h and p) . Furthermore, comparing the austenite surface states between experiments with and without SO_x inside the atmosphere, the experiments with present salt and SO_x showed an accelerated destruction behavior (Figure 5.1 l and t).

Lastly, the corrosion behavior of $Ti_{0.51}Al_{0.49}N$ and $Cr_{0.9}Si_{0.1}$ coatings deposited on austenitic steel substrates were investigated (Figure 5.2 e-l). At upper row (Figure 5.2 a-d), coatings in their as-deposited states are shown, whereas in the middle (Figure 5.2 e-h) and bottom section (Figure 5.2 i-l) the coating surfaces after LTHC and HTHC experiments are presented, respectively. For the $Ti_{0.51}Al_{0.49}N$ coated samples, the influence of Na_2SO_4/NaCl on the severity of the corrosive attack is very significant. For both coatings, $Ti_{0.51}Al_{0.49}N$ and $Cr_{0.9}Si_{0.1}$, considerable spallation of the coating and corrosion products was observed when exposed to a combination of Na_2SO_4/NaCl salt and SO_x, allowing for an accelerated attack of the austenite substrate below. Nevertheless for experiments where the coatings were only exposed to a SO_x enriched atmosphere (in absence of the salt), a better corrosion behavior was exhibited, indicated by slight changes at wide surface areas, compared to the origin state. The corrosive behavior in salt presence differ with temperature, whereas at LTHC (Figure 5.2 f and h) pitting corrosion mechanism can be surmised and for HTHC, wider areas are corroded uniformly (Figure 5.2 j and l).

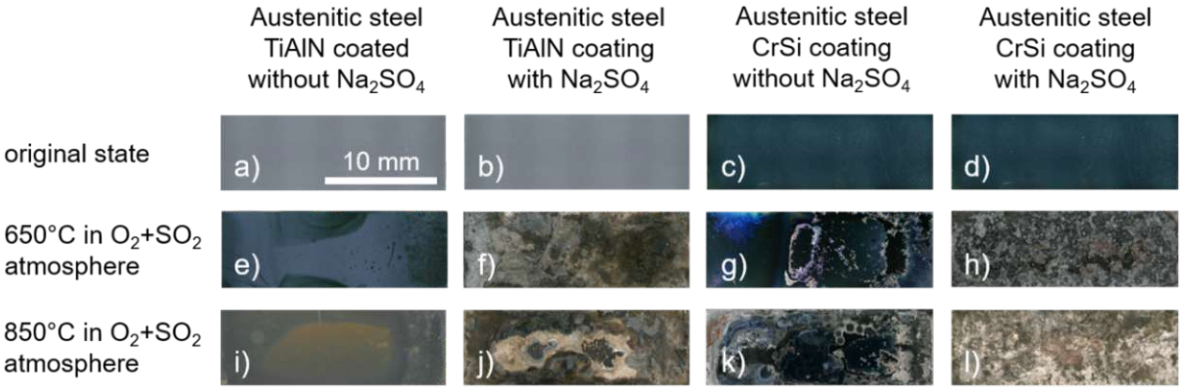

Fig. 5.2: Light microscopic study of coated austenitic steel samples, corroded with different testing parameters in top view configurations.

5.2 Structural Evolution due to HC

To determine different phases of the corroded surfaces, investigations with XRD were executed. The XRD measurements were conducted of the porous corrosion products from the IN718 and austenite substrates, as well as from the $Cr_{0.9}Si_{0.1}$ and $Ti_{0.51}Al_{0.49}N$ coatings that were exposed to SO_x with and without Na_2SO_4/NaCl at temperatures of 650°C and 850°C (Different test parameters are indicated in chapter 4.2.3). Diffractograms of the bare, uncorroded substrates serve as a reference state for subsequent comparisons with samples that have endured a corrosive process. By comparing the corroded states with the original state, conclusions about newly developed phases can be drawn and infer which reaction processes have occurred on the surfaces. The XRD patterns are measured at room temperature, so different cooling effects have to be considered.

The diffractograms for different treatments on IN718 are illustrated in Figure 5.3. In the virgin state, the matrix in IN718 is predominated by Ni, Cr and Fe and so, a combination of these elements form Ni_3Fe- and NiCr-phases (see Figure 5.3 a). In relation to Ni_3Fe and NiCr phase depletion and formation of new phases, the corrosive behavior at different conditions can be derived. At higher temperatures with SO_x inside the atmosphere, a mixture of different oxides and sulfides are developed, whereas the specific corrosion products are temperature and salt deposit dependent (Figure 5.3 b-e). Starting with the sulfidation analysis, an enhanced nickel sulfide formation develops with Na_2SO_4 deposits (Figure 5.3 c and e), which is demonstrated by the NiS_2 peak at 54° diffraction angle, whereas these phases cannot be observed in salt absence experiments (Figure 5.3 b and d).

The composition of mixed oxide layer at elevated temperature also differ with the conditions. A particularly conspicuous aspect is the appearance of Cr_7O_9 only without salt deposition – see Figure 5.3 b and d. The two high peak intensity at diffraction angles between 46° and 48° are characteristic for the Cr_7O_9 phase. The salt on the surface is suspected to prevent this phase formation. At HTHC conditions (Figure 5.3 e), strong depletion of the bare substrate matrix (Ni_3Fe and NiCr) is observed at diffraction angles of 75° and 91°. Oxidation of chromium to Cr_2O_3 is also inhibited by these conditions, whereas this oxide is preferred formed at lower temperatures (650°C, see Figure 5.3 b and c). In addition, a Fe_2NiO_4 and CrFeO formation can be observed at all experimental conditions with elevated temperatures, whereas the contents vary.

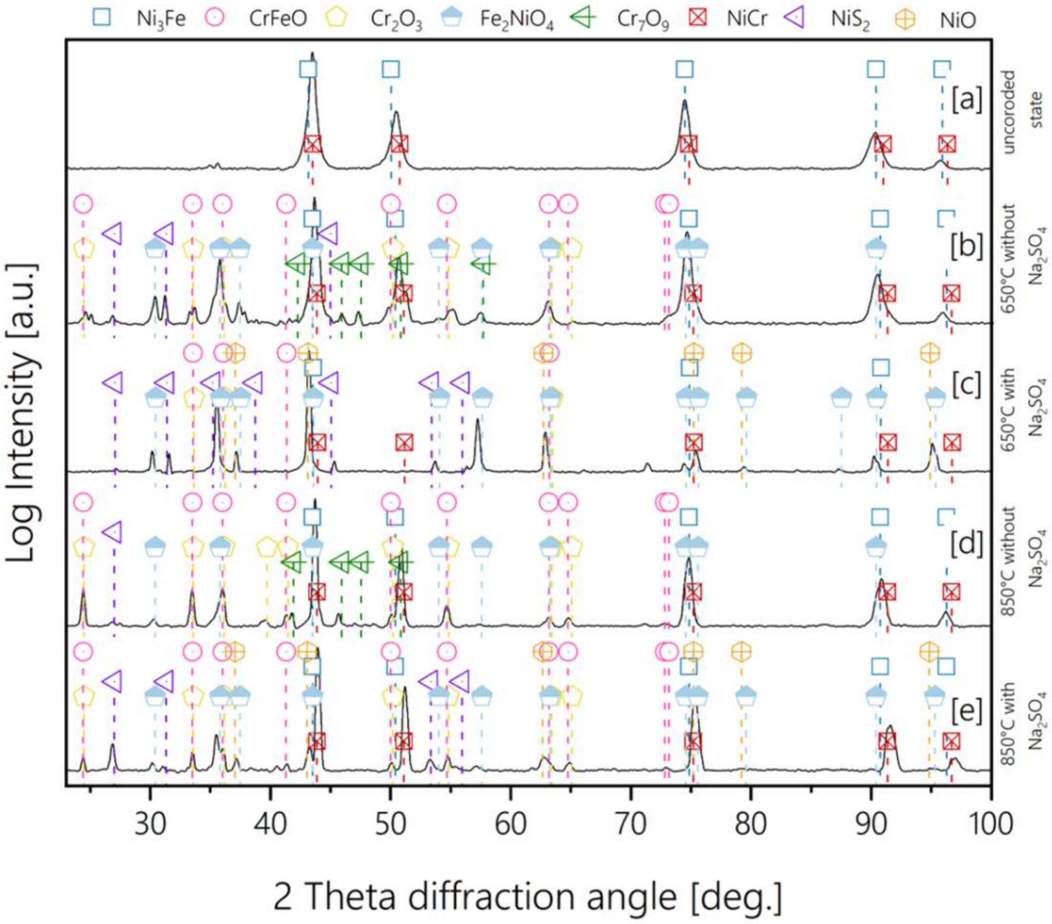

Fig. 5.3: XRD investigation at different conditions for IN718: a) uncorroded state, b) at 650°C without Na_2SO_4, c) at 650°C with Na_2SO_4, d) at 850°C without Na_2SO_4, e) at 850°C with Na_2SO_4.

For austenitic steel, a predominant γ-phase with small indications of α-phase can be indicated at origin state (Figure 5.4 a). These phases are decomposed due to LTHC and HTHC conditions with different scaling processes. The depletion of γ-austenite is predominant especially in salt deposits (Figure 5.4 c and e, at diffraction angles of 75° and 91°). The dissolution of α-ferrite is a well-known process at high temperatures and therefore, cannot be accounted to any hot corrosion processes.

High contents of Fe_2O_3 appear in particular at LTHC conditions, illustrated with intensity peaks at 24°, 85° and 88° diffraction angles in Figure 5.4 c. In SO_x atmospheres without salt deposits (Figure 5.4 b and d), the Fe_3O_4 phase formation is favored at higher temperatures (850°C), whereby a transformation from Fe_2O_3 at higher temperatures can be suspected, referred to the high intensities at 57° and 64° diffraction angle. The high content of Fe3O4 in presence of salt deposits is almost temperature independent (compared to Figure 5.4 c and e). Small contents of manganese oxide and manganese chromium oxide are also developed at elevated temperatures, see Figure 5.4 d and e.

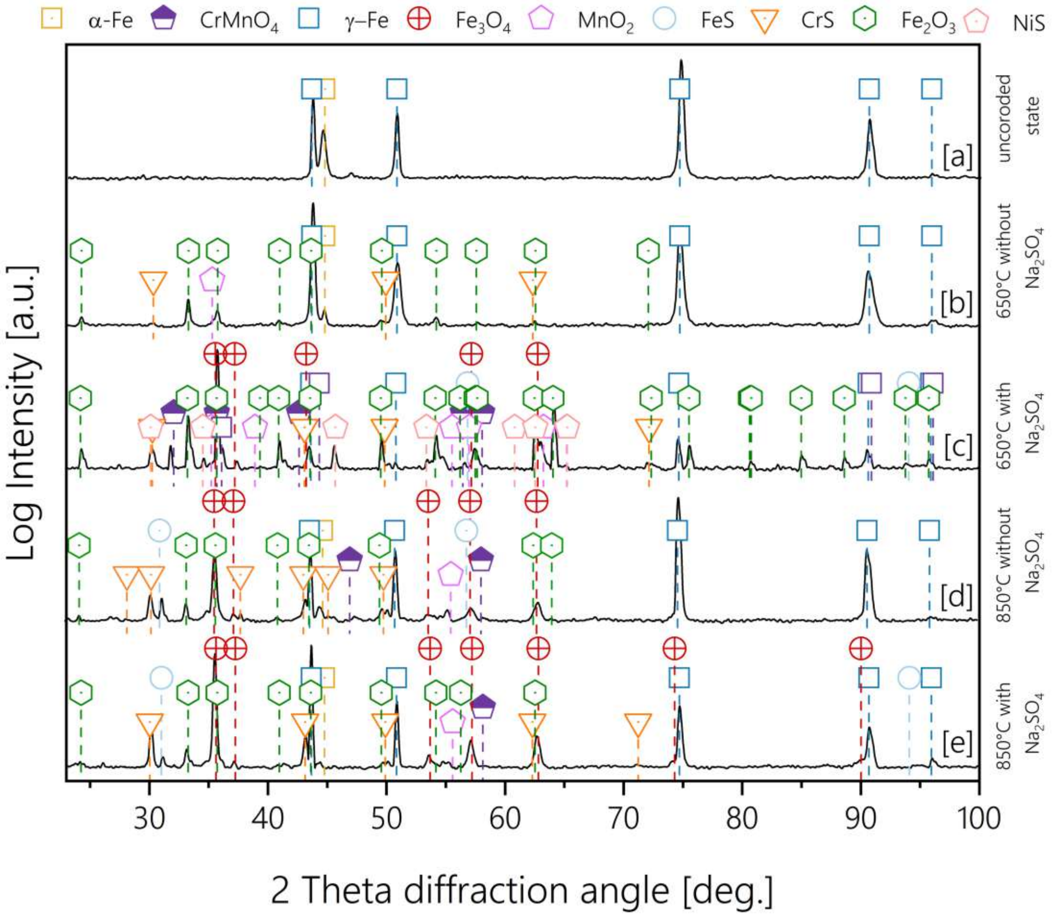

Fig. 5.4: XRD investigation at different conditions for austenitic steel: a) uncorroded state, b) at 650°C without Na_2SO_4, c) at650 °C with Na_2SO_4, d) at 850°C without Na_2SO_4, e) at 850°C without Na_2SO_4.

At high temperatures in SO_x rich atmospheres, sulfidation of chromium and iron contents occur. CrS are stabilized at these conditions, whereas presence of salt slag deposits accelerate the sulfide formations at the same temperature level, respectively, illustrated in Figure 5.4 c and e, at 30° diffraction angle. Chromium sulfidation is privileged in comparison to FeS, which keep the FeS content very low.

The as-deposited state of the $Ti_{0.51}Al_{0.49}N$ coatings, feature a γ-austenite beneath the face centered cubic structured thin film. For testing conditions without salt deposits, the peak intensity of the $Ti_{0.51}Al_{0.49}N$ layer was almost unaffected (Figure 5.5 b and d, compared to the origin state) and so, the protection was intact. Small contents of TiO_2 and Cr_2O_3 are found at higher temperatures (850°C in Figure 5.5 d between 20° and 40° diffraction angle), whereas an imperfection at the coating layer can be suspected for this oxidation process of the austenitic steel beneath the protective thin film. It can be recapituled, that the $Ti_{0.51}Al_{0.49}N$ coating is resistance in SO_x rich atmospheres without salt slags.

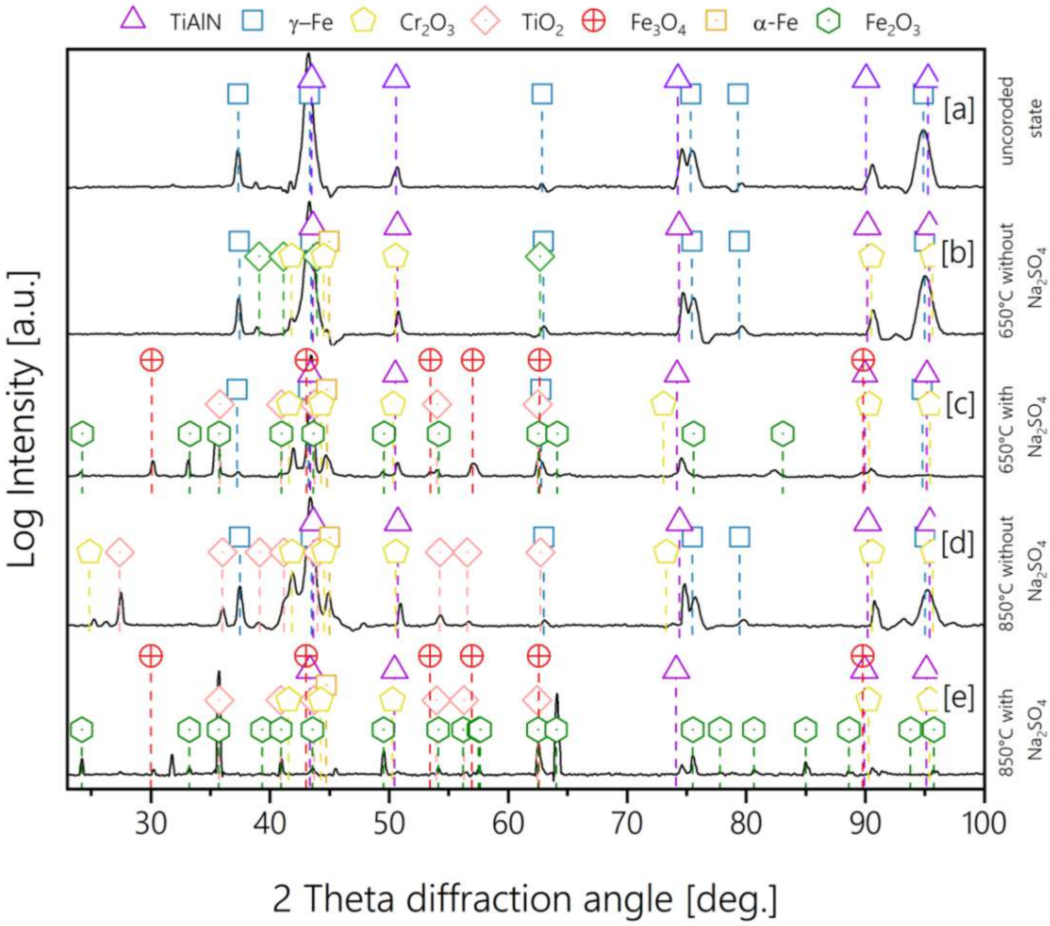

Fig. 5.5: XRD investigation at different conditions for $Ti_{0.51}Al_{0.49}N$ coated substrates: a) uncorroded state, b) at 650°C without Na_2SO_4, c) at 650°C with Na_2SO_4, d) at 850°C without Na_2SO_4, e) at 850°C with Na_2SO_4.

The situation is different at presence of salt slag deposits, as the resistance is downgraded significantly. For LTHC, small content of the $Ti_{0.51}Al_{0.49}N$ can be found in the diffractogram at 43° and 51° diffraction angle (Figure 5.5 c). Traces of Fe_2O_3, Fe_3O_4 Cr_2O_3 and TiO_2 can be indicated, leading to the interpretation that the salt deposit stringly interacts with the coating as well as the bulk material.

At HTHC conditions (Figure 5.5 e), the XRD analysis depict similar results to the austenitic steel at these conditions and so, the coating layer is vanished in the detected areas. In conclusion, the $Ti_{0.51}Al_{0.49}N$ coating failed against hot corrosion Type I.

For $Cr_{0.9}Si_{0.1}$ coatings, the resistance against SO_3 with and without salts inside the test runs is investigated in the diffractograms in Figure 5.6. Compared to the as-deposited state, the chemical state of the coating remains almost identical in absence of salt deposits (Figure 5.6 b and d) independent to the temperature applied. A moderate oxidation of chromium initiates at 850°C, which leads to the development of Cr_2O_3 scales (e.g. at 24° and 33° diffraction angle in Figure 5.6 d).

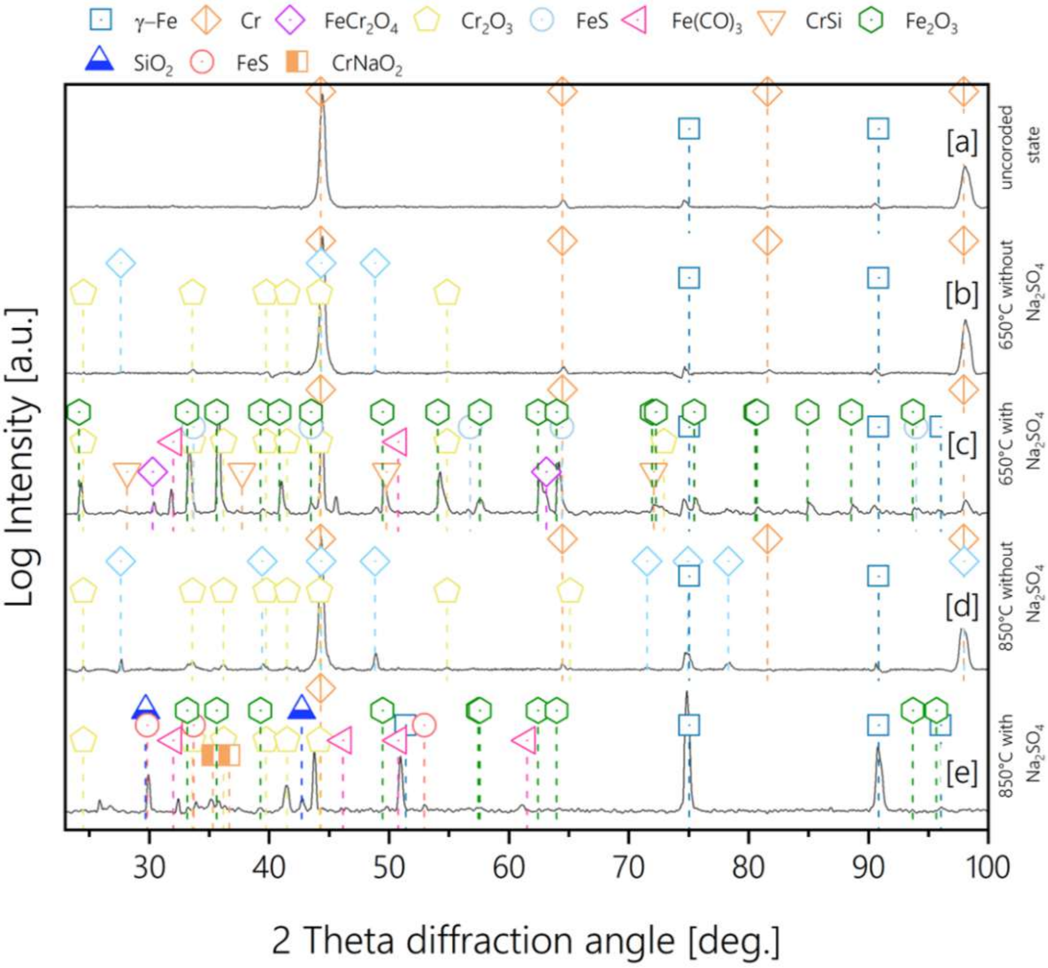

Fig. 5.6: XRD investigation at different conditions for $Cr_{0.9}Si_{0.1}$ coated substrates: a) uncorroded state, b) at 650°C without Na_2SO_4, c) at 650°C with Na_2SO_4, d) at 850°C without Na_2SO_4, e) at 850°C with Na_2SO_4.

Furthermore, under LTHC and HTHC conditions, the $Cr_{0.9}Si_{0.1}$ coating suffers severe corrosive transformations. Iron oxides in surface near areas evolve, indicating that the corrosive process has already destroyed the $Cr_{0.9}Si_{0.1}$ protective barrier and therefore, enabled direct attack on the bulk material. Also, oxidation of the coating components constitutes the corrosion of the thin $Cr_{0.9}Si_{0.1}$ film, leading to Cr_2O_3 peaks in the diffractogram (e.g. at diffraction angle 42° in Figure 5.6 c and e). The Si content inside the thin film is oxidized at HTHC conditions, illustrated with different peak intensities at diffraction angles of 30° and 43° in Figure 5.6 e.

The destructive pattern at hot corrosion Type I terms are similar with the results gained for uncoated and $Ti_{0.51}Al_{0.49}N$-coated austenitic steel and so, hot corrosion Type I is very destructive for all sample modifications in the same manner. Indicative for the $Cr_{0.9}Si_{0.1}$ layer removal is the non-present peak at 98° diffraction angle at HTHC conditions (Figure 5.6 e), compared to the uncorroded state (Figure 5.6 a).

5.3 Morphological Investigations

The morphology of the bare substrates and coated samples was investigated after corrosive attack by SEM and EDS. The SEM analysis clearly shows that the corrosion mechanism changes with the presence of salt deposits and temperature for both bulk materials (Figure 5.7 a to l).

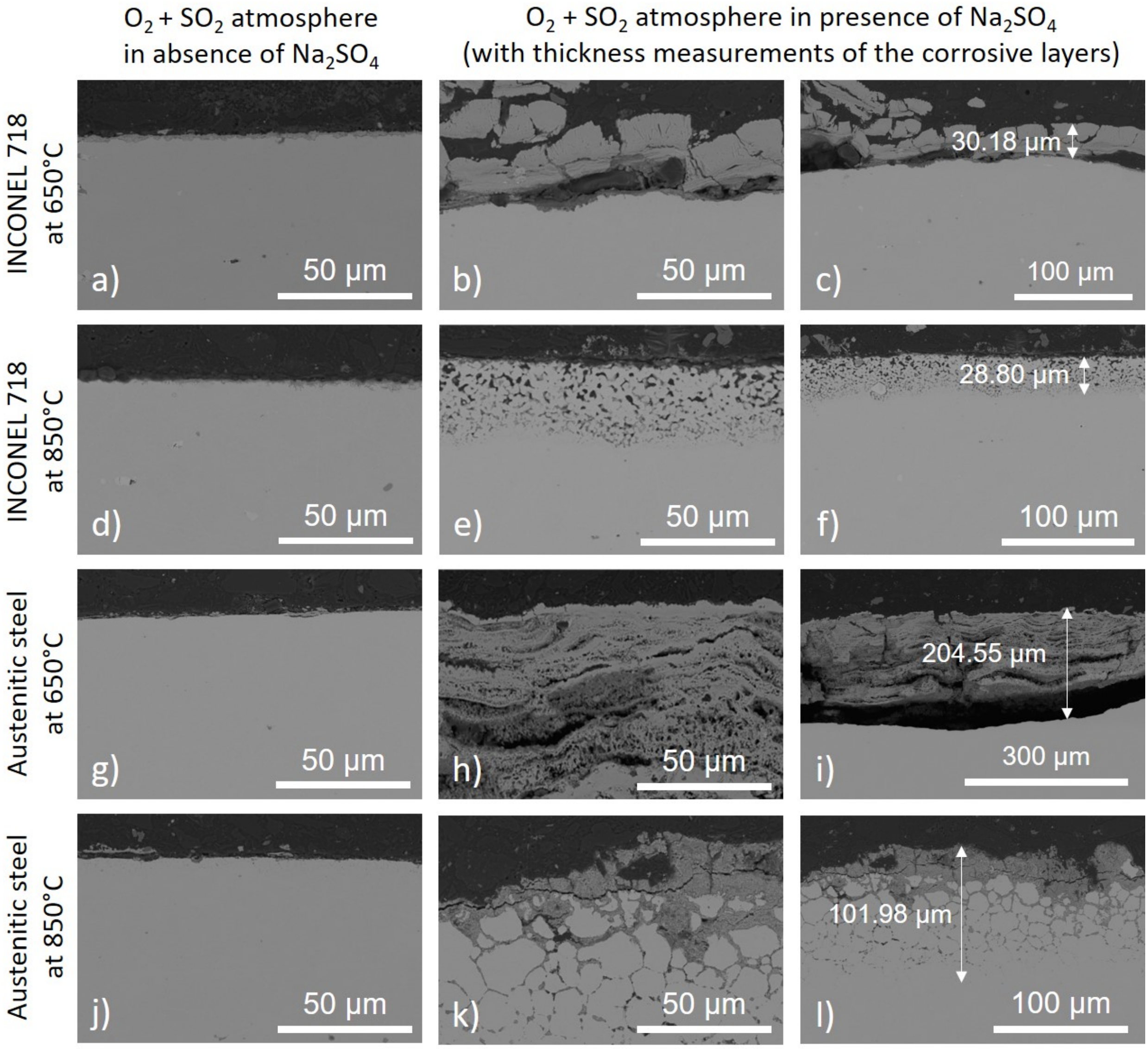

Fig. 5.7: Cross sectional SEM investigations of bulk materials without protective coatings at different temperatures in absence or presence of Na_2SO_4 salt slags.

IN718 and austenite are resistant materials against high temperature oxidation, where they readily develop protective oxide scales protecting them from further oxidative attack (left column of Figure 5.7). This behavior, however, drastically changes in hot corrosion environment, where the damage occurs in combination of an aggressive oxidation atmosphere and a salt deposit. Under these conditions, the destruction process accelerates and can easily proceed deep into the material (Figure 5.7 middle column). Especially in austenitic steel, the corrosive attack was uninhibited see Figure 5.7 h and k. Both materials suffer tremendously under LTHC and/or HTHC conditions. To emphasize the impact of salt deposit in combination with a SO_x rich atmosphere, the proportions of the corrosive layer can be compared to the experiments, where substrates were solely exposed to the SO_x rich gas (Corrosion thickness measurements at the right column of Figure 5.7). For IN718, the corrosion layer thickness is approximately 15 times higher when salt was present during the corrosion experiment, and for austenitic steel the impact was even higher. Based on the theoretical background in chapter 2.2.1 and 2.2.2, at LTHC conditions an corrosive process only occurs on surface near regions and in contrast, HTHC shows significant inner corrosion events toward the substrate morphology for both bulk materials.

In Figure 5.8, SEM cross sections of as-deposited $Ti_{0.51}Al_{0.49}N$ and $Cr_{0.9}Si_{0.1}$ on silicon substrates are presented. The layer thicknesses of the protective coatings are about 4.2μm for $Ti_{0.51}Al_{0.49}N$ and 4.1μm for $Cr_{0.9}Si_{0.1}$, compared to Figure 5.8. Both coatings exhibit a highly dense and columnar morphology. In addition, the arc evaporated $Ti_{0.51}Al_{0.49}N$ coatings obtains a rougher surface as growth defects, such as droplets are presented – compared to a very smooth surface of the $Cr_{0.9}Si_{0.1}$ deposited via HiPIMS.

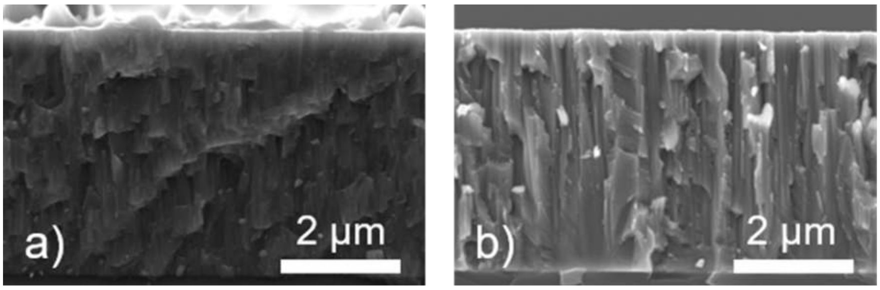

Fig. 5.8: a) Cross-section of $Ti_{0.51}Al_{0.49}N$ in as-deposited state and b) Cross-section of $Cr_{0.9}Si_{0.1}$ in as-deposited state.

In Figure 5.9 the corrosive of the coated substrates is presented. For atmospheres without any salt mixtures, the coatings stay protective and no significant corrosion can be seen (left column of Figure 5.9). Therefore, the deposition of thin films on the surface can protect the bulk materials in absence of salt mixtures inside the atmosphere.

For experiments with Na_2SO_4/NaCl, the results change significantly. For $Ti_{0.51}Al_{0.49}N$ coated samples under LTHC conditions (650°C), it is evident that the attack starts at metallic defect sites (droplets) within the coating and propagates to the underlying material (Figure 5.9 b). Nevertheless, under LTHC conditions at 650°C, the $Ti_{0.51}Al_{0.49}N$ coatings showed good corrosion behavior, where the corrosive attack was only observed at defect sites, which enabled a direct attack of the austenite surface.

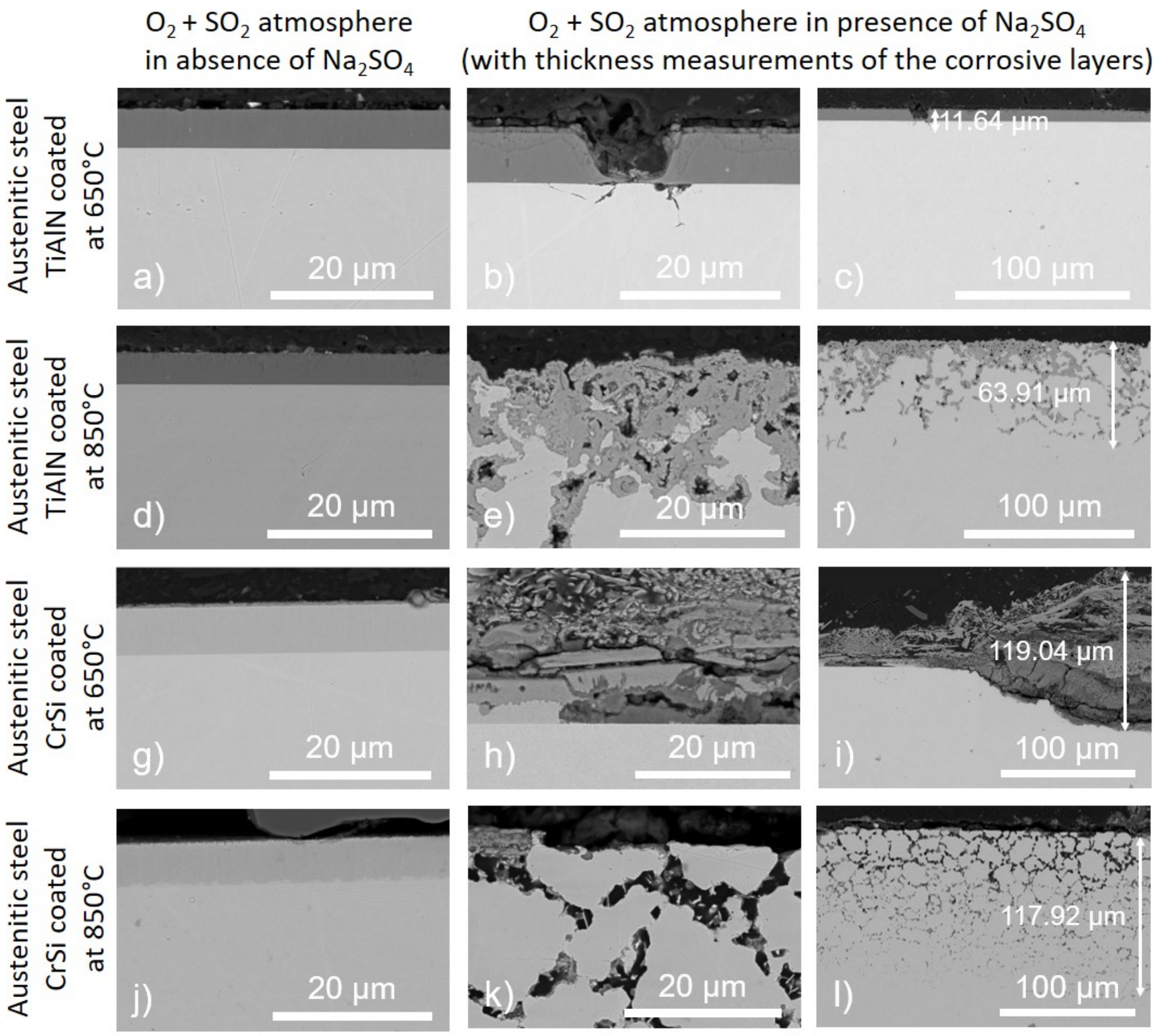

Fig. 5.9: SEM investigations of coated samples at different temperatures and in absence or presence of Na_2SO_4.

Under HTHC conditions (850 °C with salt deposits), the $Ti_{0.51}Al_{0.49}N$ coating succumbed at the aggressive media. The corrosive attack advanced deep into the interior of the underlaying bulk material (Figure 5.9 e). Compared to the original as-deposited state (4.2μm), the thickness of the corrosion products is multiple times higher. For $Ti_{0.51}Al_{0.49}N$ samples, the corrosive process reaches a maximum depth of 64μm (Figure 5.9 f)

Contrary to the corrosion resistance of the $Ti_{0.51}Al_{0.49}N$ coating, the $Cr_{0.9}Si_{0.1}$ coatings, however, showed little resistivity against the aggressive nature of the salt deposits at 650°C, allowing the corrosion process to occur more aggressively (Figure 5.9 h). The corrosion of $Cr_{0.9}Si_{0.1}$ exhibited broad areas of spallation, where accelerated corrosive attack causes catastrophic results, leading to a corroded layer thickness of 119μm (Figure 5.9 i). At higher temperatures (850°C), the corrosion process attacks the material at deeper areas, which can be referred as inner sulfidation at HTHC (referred to the theoretical background in chapter 2.2.1), illustrated in Figure 5.9 k. Here a selective attack of grain boundary interior is predominant. The $Cr_{0.9}Si_{0.1}$ the attack reached up to 118μm, which is presented in Figure 5.9 l.

In order to analyze the chemical composition of the tested coatings, EDS line scans were utilized. The position of the line scans was determined by SEM measurements. The results of EDS analysis of the coated samples are illustrated in Figure 5.10 and Figure 5.11 and will be discussed for the experimentally corroded $Ti_{0.51}Al_{0.49}N$- and $Cr_{0.9}Si_{0.1}$-coatings, respectively.

Starting with the $Ti_{0.51}Al_{0.49}N$ coating, at 650°C without salt atmosphere in the testing process (Figure 5.10 a), the coating remains almost unaffected. In comparison to the corrosion experiments with salt deposits the devastating effect of $Na_2SO_4/NaCl$ becomes clear (Figure 5.10 b). The salt deposit together with the SO_x rich atmosphere achieve a quite significant breakdown of the nitride-based coating. The content of Al is decreased on surface near areas and substantial oxygen diffusion can be registered throughout the coating, forming mixed oxides.

The same behavior can also be observed at 850°C (Figure 5.10 c and d). It was also noticed, that in absence of a salt deposit, the $Ti_{0.51}Al_{0.49}N$ coating developed a mixed titanium-aluminum oxide scale with formations of Al_2O_3 at the outer-most parts of the coating and directly beneath, a titanium oxidic layer [41]. For 650°C experiments at identical SO_x concentration without salt deposits, this oxidic formations were not observed. Under HTHC conditions in presence of salts, the corrosive process occurs to such extend that the $Ti_{0.51}Al_{0.49}N$-coating cannot protect the underlying substrate material and an unhindered attack of the austenite is observed. The experimental results under HTHC conditions produced porous oxide scales where neither a clear oxide-coating interface, nor a coating-substrate interface could be identified, see Figure 5.10 d. This leads to the assumption, that the deposited coating material has spalled off entirely or it has deteriorated and fused with the salt deposit.

The $Cr_{0.9}Si_{0.1}$ coating stays almost unaffected in absence of salt deposits at 650°C, (Figure 5.11 a). At LTHC conditions with salt deposition, a depletion of chromium started in the outer regions of the coating, whereas a part of the protective coating is still present – see Figure 5.11 b. It seems to be right in inferring that the $Cr_{0.9}Si_{0.1}$ is not supremely resistant against LTHC, but the corrosive attack is slowed down. At higher temperatures (850°C) without salt deposits, the coating system is factual resistant, with very low reactions onto the surface (Figure 5.11 c). For HTHC conditions with salt presence (Figure 5.11 d), the coating is not existing anymore and a porous iron oxide layer is formed. Inside this layer, the chromium content is lowered to a minimum, so no protective scale can be developed anymore.

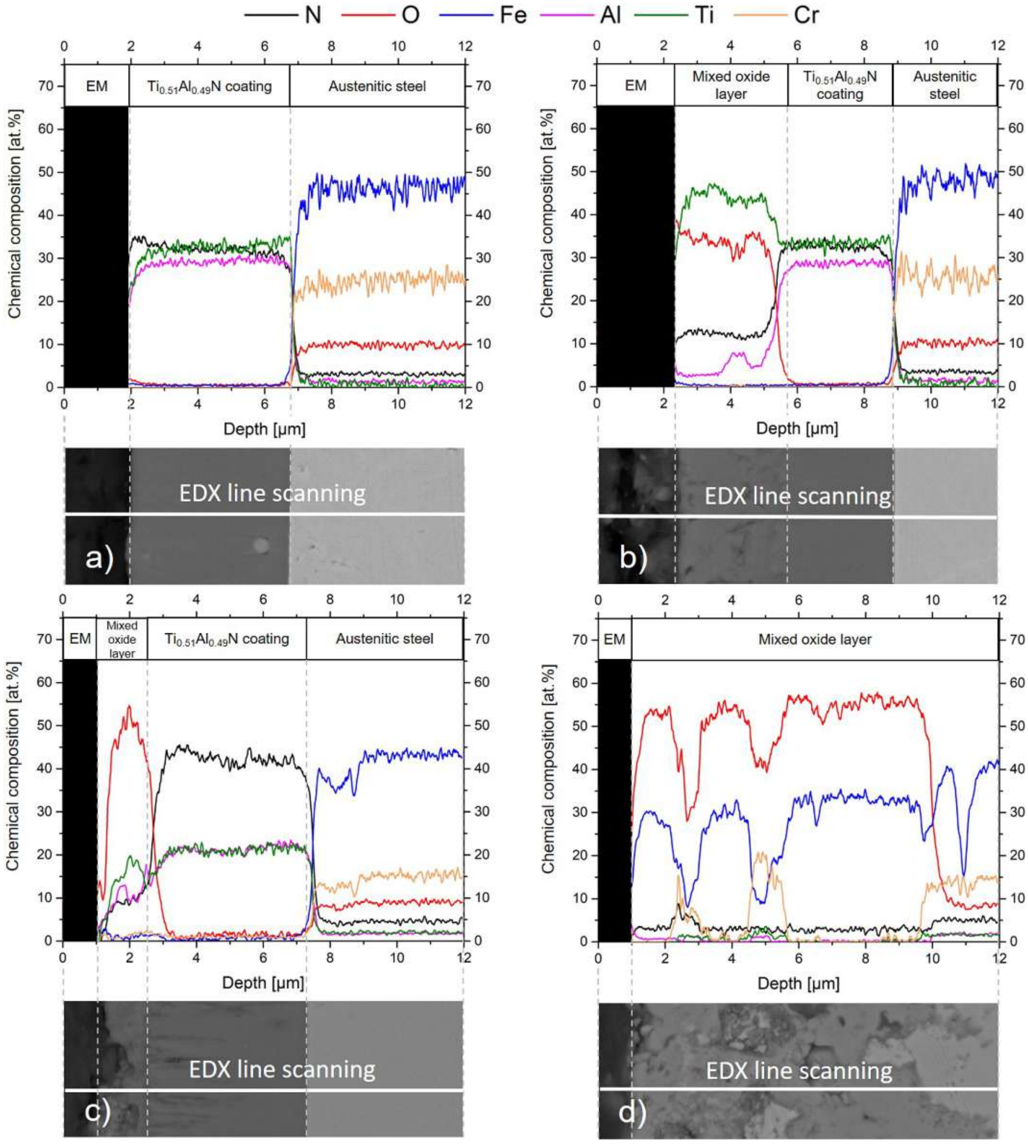

Fig. 5.10: EDS line scans of $Ti_{0.51}Al_{0.49}N$ coatings on austenitic steel with following conditions: a) 650°C without Na_2SO_4, b) 650°C with Na_2SO_4, c) 850°C without Na_2SO_4, d) 850°C with Na_2SO_4.

Under consideration of the SEM results and EDS line scans from Figure 5.11, it can be concluded, that the attack on $Cr_{0.9}Si_{0.1}$ coatings is highly dependent on the presence of salt mixtures inside the atmosphere, due to the strong corrosive attack at LTHC and HTHC conditions.

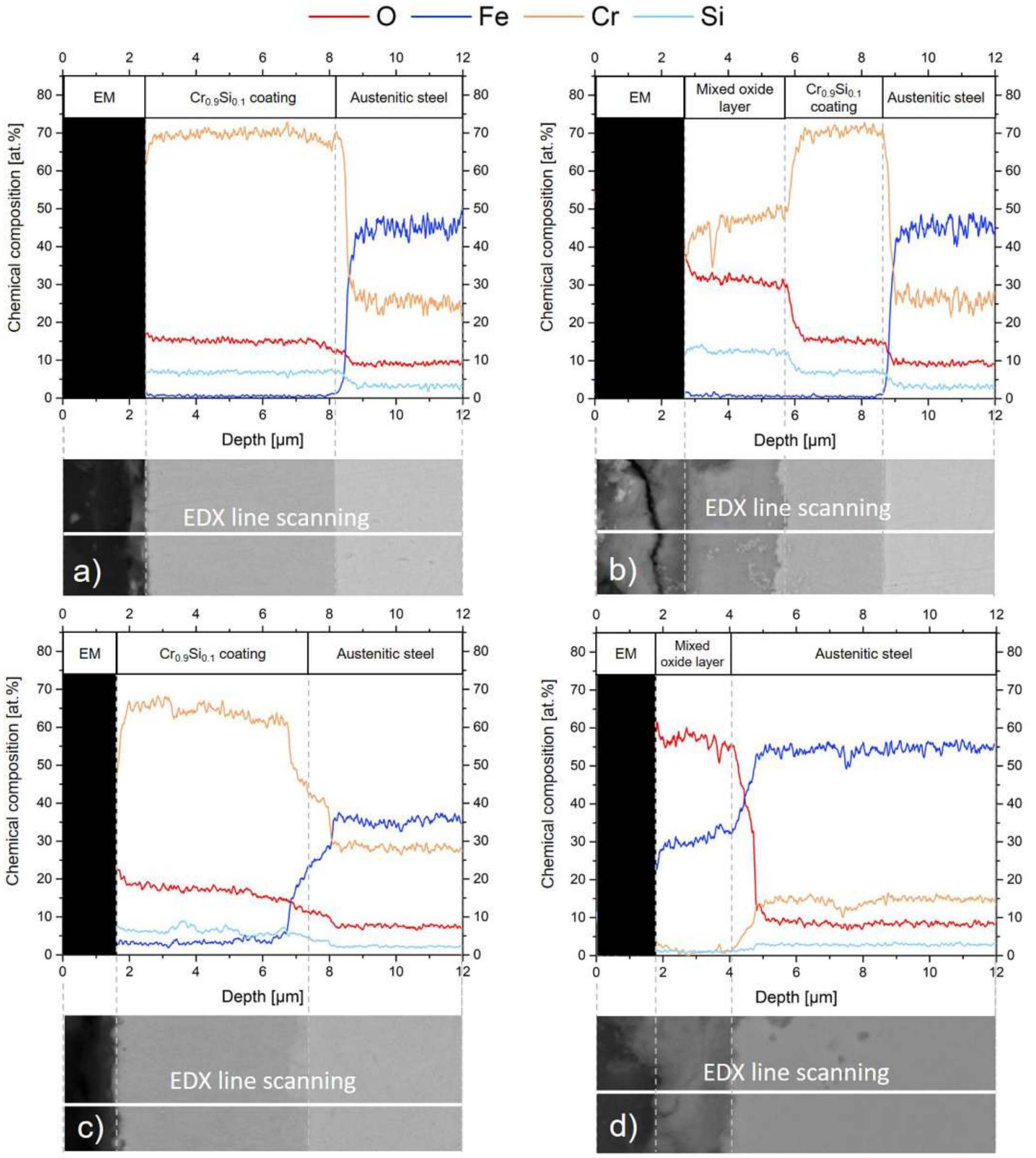

Fig. 5.11: EDS line scans of $Cr_{0.9}Si_{0.1}$ coatings on austenitic steel with following conditions: a) 650°C without Na_2SO_4, b) 850°C without Na_2SO_4, c) 650°C with Na_2SO_4, d) 850°C with Na_2SO_4.

In conclusion, it can be inferred that noticeable improvement in the corrosion behavior was exhibited by the coated samples. Especially under LTHC conditions, a significant degree of corrosion protection was seen, where the coating material withstood the attack without breaching. Therefore, physical vapor deposition coatings represent a promising strategy in high temperature applications where hot corrosion is a frequent issue.

Chapter 6

Conclusion & Outlook

Hot corrosion is a common phenomenon in post-combustion sections of gas turbines, which describes the accelerated oxidation of metals and alloys in the presence of salt-deposits. While hot corrosion of Ni-based super alloys has gained much attention by aviation industries and its revolving scientific community over the last few decades, available literature on corrosion protective coatings and their testing on a laboratory scale has remained scarce. From this standpoint, this thesis presented the conceptualization and construction of an application-orientated lab-scale hot corrosion testing-rig. A derivation of its theoretical design, which highlights key components that play an essential role for successfully executing hot corrosion experiments (LTHC Type I at ∼650°C and HTHC Type II at ∼850°C), was discussed in detail. An extensive literature review was employed for providing fundamental principles about the conditions and experimental parameters, that need to be met for simulating hot corrosion processes.

The Corrosion Oven for Research and technical Applications (CORA) was conceptualized in three segments:

(i) A gas-mixing unit for transporting individual gas-components and synthesizing the corrosive atmosphere as needed, SO_2, O_2 and Ar were chosen as gas-constituents for the experimental atmosphere. Whereas SO_2 and O_2 (as well as SO_3, which forms within the reactor tube) are the components that actively contribute to the hot corrosion process, Ar solely functioned as an inert carrier gas and dilution component. Due to kinetic constraints of the SO_2 to SO_3 conversion, which has proven to be a key factor in the LTHC mechanism, the final gas mixture was flown over an iron-oxide catalyst to accelerate the reaction.

(ii) A reaction chamber for controlling and safely confining the corrosion reactions (comprised of a three-zone gradient furnace and a quartz flow-reactor tube). In order to accommodate experimental conditions that support both LTHC and HTHC mechanisms, a furnace capable of reaching 1100°C was chosen. Furthermore, three independently working heating zones were calibrated, for an optimized control of the reaction conditions within the quartz-reactor. With the gas mixture entering the reactor tube within the furnace, it encounters the first heating zone (Zone 1). Here, the temperature was set, not only for the purpose of pre-heating the gases before they arrive at the samples, but also to thermodynamically and kinetically promote the conversion of SO_2 to SO_3 in the most effective way. After Zone 1, the gases encounter the samples of interest (Zone 2), where the temperature was set for the desired hot corrosion type (600-850°C for LTHC, and 750-950°C for HTHC). Here, a fine-sintered alumina-silica substrate holder was positioned, which accommodates testing samples. Samples were positioned either 'vertically with no Na_2SO_4/NaCl salt-depositions or positioned 'horizontally' with salt-depositions. After Zone 2, the atmosphere travels downstream through a cooling passage (Zone 3), where the gases cool down before they were guided through the gas-analysis segment.

(iii) An analytical segment for screening and quantifying the gas composition after the reaction chamber. After exiting the reactor chamber, the gases enter the last segment of CORA, the analytical unit. With an integrated EPA-Method 8 system, the atmosphere can be analyzed for its SO_2 and SO_3 concentration, thus providing crucial information about the reaction mechanism and corrosion conditions within the reaction chamber.

As a final step, the testing capability of CORA was assessed, through an array of hot corrosion experiments involving industrially relevant bulk materials, such as IN718 and austenitic steel, as well as $Cr_{0.9}Si_{0.1}$ and $Ti_{0.51}Al_{0.49}N$ coated austenite substrates. An atmosphere consisting of 1000 ppm SO_2 with an oxygen ratio of 150:1 was kept identical for all experiments. All samples were tested under LTHC conditions (Zone 1 = 650°C/Zone 2 = 650°C) as well as under HTHC conditions (Zone1 = 650°C/Zone 2 = 850°C), containing both, sample arrangements with Na_2SO_4/NaCl deposits, as well as samples without deposits. By utilizing analytical techniques, such as SEM, EDS and XRD, the aggressive salt-slag induced breakdown of the coating materials, as well as the accelerated deterioration of the IN718 and austenite surface structure was observed. Typical porous oxide scale growth in combination with interior metal sulfide phase formations imply the presence of a hot corrosion mechanism. Despite good corrosion behavior of both $Cr_{0.9}Si_{0.1}$ and $Ti_{0.51}Al_{0.49}N$ coatings in absence of any slat-deposit, their ability to exhibited superior corrosion behavior under LTHC or HTHC conditions (when in contact with salt deposits) could not be shown.

In conclusion, further research has to be dedicated to investigating more suitable material systems as candidates for hot corrosion protective coatings. CORA has shown to be an effective tool in providing highly aggressive HC conditions on a laboratory scale. Future work with CORA will hopefully help to fully explore the potential of PVD coatings as a protective strategy in gas-turbines, whilst providing valuable data for science to come.

Bibliography

[1] A. James and S. Rajagopalan, in *Structural Alloys for Power Plants* (Elsevier, 2014) pp. 3–21.

[2] H. J. Maier, T. Niendorf, and R. Bürgel, *Handbuch Hochtemperatur-Werkstofftechnik* (Springer Fachmedien Wiesbaden, Wiesbaden, 2019).

[3] R. A. Rapp, Corrosion Science **44**, 209 (2002).

[4] C. A. C. Sequeira, *High Temperature Corrosion* (John Wiley & Sons, Inc., Hoboken, NJ, USA, 2019) pp. 340–360.

[5] M. Spiegel, in *Encyclopedia of Electrochemistry* (Wiley, 2003).

[6] E. Akca and A. Gürsel, Periodicals of Engineering and Natural Sciences (PEN) **3** (2015).

[7] V. Mannava, A. S. Rao, N. Paulose, M. Kamaraj, and R. S. Kottada, Corrosion Science **105**, 109 (2016).

[8] B. N. Popov, in *Corrosion Engineering* (Elsevier, 2015) pp. 481–523.

[9] C. Zhou and Y. Song, in *Thermal Barrier Coatings* (Elsevier, 2011) pp. 193–214.

[10] C. Leyens, I. G. Wright, and B. A. Pint, Oxidation of Metals **54**, 401 (2000).

[11] H. Xu, H. Guo, and S. Gong, in *Developments in High Temperature Corrosion and Protection of Materials* (Elsevier, 2008) pp. 476–491.

[12] B. Cottis, M. Graham, R. Lindsay, S. Lyon, T. Richardson, D. Scantlebury, and H. Stott, *Corrosion Engineering, Science and Technology* (Elsevier, 2010).

[13] R. W. Revie and H. H. Uhlig, *Spectroscopy* (John Wiley & Sons, Inc., Hoboken, NJ, USA, 2008) p. 441.

[14] B. N. Popov, in *Corrosion Engineering* (Elsevier, 2015) pp. 29–92.

[15] G. Palumbo, Physical Sciences Reviews **1**, 1 (2016).

[16] B. N. Popov, in *Corrosion Engineering* (Elsevier, 2015) pp. 365–450.

[17] A. Sedriks and O. Zaroog, in *Reference Module in Materials Science and Materials Engineering* (Elsevier, 2017).

[18] H. Kaesche, *Die Korrosion der Metalle* (Springer Berlin Heidelberg, Berlin, Heidelberg, 2011).

[19] A. S. Khanna, in *Handbook of Environmental Degradation of Materials*, Vol. 2 (Elsevier, 2018) pp. 117–132.

[20] B. Salehnasab, E. Poursaeidi, S. Mortazavi, and G. Farokhian, Engineering Failure Analysis **60**, 316 (2016).

[21] S. Caines, F. Khan, and J. Shirokoff, Journal of Loss Prevention in the Process Industries **26**, 1466 (2013).

[22] R. Burgel, J. Grossmann, O. Lusebrink, H. Mughrabi, F. Pyczak, R. Singer, and A. Volek, in *Superalloys 2004 (Tenth International Symposium)* (TMS, 2004) pp. 25–34.

[23] R. A. Rapp and Y.-S. Zhang, JOM **46**, 47 (1994).

[24] B. S. Lutz, J. M. Alvarado-Orozco, L. Garcia-Fresnillo, and G. H. Meier, Oxidation of Metals **88**, 599 (2017).

[25] R. A. Rapp, CORROSION **42**, 568 (1986).

[26] J. M. Alvarado-Orozco, J. E. Garcia-Herrera, B. Gleeson, F. S. Pettit, and G. H. Meier, Oxidation of Metals **90**, 527 (2018).

[27] D. E. Winterbone and A. Turan, in *Advanced Thermodynamics for Engineers* (Elsevier, 2015) pp. 307–322.

[28] R. C. Brown, M. R. Anderson, R. C. Miake-Lye, C. E. Kolb, A. A. Sorokin, and Y. Y. Buriko, Geophysical Research Letters **23**, 3603 (1996).

[29] D. Fleig, K. Andersson, F. Normann, and F. Johnsson, Industrial & Engineering Chemistry Research **50**, 8505 (2011).

[30] Y. Sarbassov, L. Duan, V. Manovic, and E. J. Anthony, Greenhouse Gases: Science and Technology **8**, 402 (2018).

[31] L. P. Belo, L. K. Elliott, R. J. Stanger, R. Spörl, K. V. Shah, J. Maier, and T. F. Wall, Energy & Fuels **28**, 7243 (2014).

[32] EPA, United States Environmental Protection Agency **4**, 1923 (2019).

[33] I. Gurrappa, Materials and Manufacturing Processes **15**, 761 (2000).

[34] J. Stringer, Le Journal de Physique IV **03**, C9 (1993).

[35] MKS Instruments, "Massflow controller GE50A," (2020).

[36] JEVATEC, "JEVAflow FCU-4 control panel," (2020).

[37] Carbolite Gero, "Temperature profile of a three-zone gradient tube furnace," (2020).

[38] A. A. Bunaciu, E. gabriela Udriştioiu, and H. Y. Aboul-Enein, Critical Reviews in Analytical Chemistry **45**, 289 (2015).

[39] Y. Leng, in *Materials Characterization* (Wiley-VCH Verlag GmbH & Co. KGaA, Weinheim, Germany, 2013) pp. 127–161.

[40] S. Henning and R. Adhikari, in *Microscopy Methods in Nanomaterials Characterization* (Elsevier, 2017) pp. 1–30.

[41] H. Riedl, D. Holec, R. Rachbauer, P. Polcik, R. Hollerweger, J. Paulitsch, and P. H. Mayrhofer, Surface and Coatings Technology **235**, 174 (2013).